Multiscale Computational Modelling of Nano-Silica Reinforced Cement Paste: Bridging Microstructure and Mechanical Performance

Mylvaganam Nithurshan [1], Yogarajah Elakneswaran [1, *], Yuya Yoda [2], Ryoma Kitagaki [1], and Naoki Hiroyoshi [1]

[1] Graduate School of Engineering, Hokkaido University

Sapporo-shi, Hokkaido 060-8628, Japan

[2] Shimizu corporation

Shimizu Institute of Technology

Center for Construction Engineering, Japan

* Corresponding author

E-mail: elakneswaran@eng.hokudai.ac.jp (Y. Elakneswaran)

Tel: +81-11-706-7274

Abstract

This study presents a systematic model to optimise nano-silica utilisation in cement paste and predict its nonlinear behaviour. The model integrates a hydration model, which calculates the dissolution rate of each clinker mineral, with a thermodynamic model that simulates the hydration reaction and interaction between hydrates and nano-silica. The investigation considered different replacement levels of nano-silica (2 and 4% by weight of cement) to analyse the phase assemblages and porosity of nano-silica reinforced cement paste. The reaction between nano-silica and the hydrate (portlandite) was meticulously accounted for by incorporating the formation of calcium-silica-hydrate (C-S-H) with a realistic transition from jennite-type C-S-H (Si/Ca ratio of 0.58) to tobermorite C-S-H (Si/Ca ratio of 0.67). The coupled model was validated against the experimental results obtained from thermogravimetric analysis, X-ray diffraction, and scanning electron microscopy, ensuring its reliability. Subsequently, the model was used to compute the volume fractions of various phases including hydrates, unhydrated clinkers, pores, and unreacted nano-silica. A representative volume element (RVE) was formulated for the cement pastes with and without nano-silica using MATLAB. The RVE was further evaluated through finite element analysis using COMSOL Multiphysics, enabling the computation of homogenised material properties such as compressive strength, and this aligned well with experimental findings. In summary, the proposed systematic model provides a realistic prediction of the nonlinear behaviour of cement pastes with different nano-silica replacement levels. Its applicability extends to the optimisation of cement-based composites for diverse engineering applications.

Keywords: Nano-silica, cement paste, hydration model, thermodynamic model, representative volume element, finite element analysis

1. Introduction

The growing demand for durable and sustainable construction of buildings and infrastructure has spurred a focus on high-performance cement-based materials [1]. Supplementary cementitious materials (SCMs) such as nano-silica are gaining popularity in the construction industry because of their ability to enhance durability, strength, and sustainability [2]. The high reactivity and small particle size make nano-silica particularly attractive for applications requiring rapid strength development [3]. Nano-silica in cement-based materials acts as a nucleation site, which promotes the hydration of clinker minerals and pozzolanic materials; during this process, calcium hydroxide reacts with nano-silica to form calcium silicate hydrate (C-S-H) gel [4]. Consequently, the microstructure becomes denser, possessing a higher strength than that without incorporating nano-silica [5].

Nano-silica has been effectively combined with various additives and SCMs, such as fly ash [6,7], slag [8,9], glass powder [10], metakaolin clay [11], and calcined clay [12], in construction industries to enhance the performance of cement-based materials. For instance, Hou et al. [13] demonstrated that the pozzolanic reaction of colloidal nano-silica and its nucleation occurred rapidly in fly ash mortar, particularly at a very early age, compared with the addition of the same quantity of silica fume. The addition of 5% colloidal nano-silica increased the compressive strength of the fly ash mortar by 45 and 12% on days 7 and 28, respectively. However, at later ages, the acceleration effect of nano-silica diminished. Therefore, the effectiveness of nano-silica in cement-based materials varies depending on its properties, such as particle size and morphology, specific dosage, and incorporation method. For instance, Meng et al. [14] examined the microstructural transformation of cement pastes with different nano-silica particle sizes (15 and 50 nm) using X-ray diffraction (XRD), scanning electron microscopy (SEM), and thermogravimetric analysis (TGA). The results revealed that larger nano-silica particles demonstrated superior compressive strength compared to smaller nano-silica particles. In addition, nano-silica with a smaller particle size resulted in a denser microstructure with a reduced average pore size. Moreover, nano-silica morphology affects the characteristics of cement

mixtures. Colloidal nano-silica considerably lowered the workability of cement mixtures compared to silica gel and silica fume, owing to the high absorption of free water and agglomeration of nano-silica particles in the cement composite [15].

Appropriate quantities of nano-silica are required to achieve excellent outcomes and compatibility with the other cementitious materials used in cement composites [4]. According to literature, nano-silica has been utilised as an additive or replacement in cementitious materials at various dosages, ranging from 0.5% to 7% in cement pastes [16–18], 1% to 12% in mortar [13,16,19], and 0.5% to 10% in concrete [4,20]. However, determining the ideal replacement level and properties of nano-silica combined with different SCMs is laborious and time-consuming. Therefore, there is a demand for a model that can predict the appropriate properties of nano-silica, accounting for the chemical and physical characteristics of the cementitious materials with which it interacts. This predictive model aids in making decisions regarding material selection and predicting the performance for future applications.

Recent studies have explored various techniques to predict the optimal utilisation of nanoparticles and mechanical characteristics of cement-based composites. These include analytical approaches, [21] machine learning methods [22], and microstructural models [23,24]. Among these, microstructure models have emerged as widely accepted and effective for precisely forecasting optimal dosages and mechanical performance, because machine learning and analytical techniques rely purely on historical data [25] and often struggle to account for complicated composite materials. Microstructural models accurately simulate the hydration processes of cementitious materials [23,24]and concurrent evolution of the microstructure, which are crucial factors influencing the mechanical properties of cement-based materials. Notably, microstructure models like HYMOSTRUC [26], CEMHYD3D [24], μic [23], and DuCOM [27] have capably predicted cementitious material hydration dynamics but have fallen short in accurately projecting the mechanical properties [25]. Recently, there has been growing interest in computational homogenisation methods and multiscale finite element simulations. These methods accurately capture

micromechanical stress-strain behaviour. Finite element modelling based on representative volume elements (RVEs) provides great flexibility in configuring microstructures, making it a valuable approach for assessing composite material properties [28].

Considering the necessity for optimisation tools applicable to SCMs, such as nano-silica, and prediction of nonlinear behaviour in cement-based materials, this study introduces a microscale finite element model integrated with hydration and thermodynamic models. This approach initially integrates cement hydration and thermodynamic models to predict microstructural changes in volume fractions (hydrates, unhydrated clinker, pores, and unreacted nano-silica). The strength evolution of the cement pastes with and without nano-silica incorporation are then computed using finite element analysis. The proposed model was validated from the results of an experimental investigation, in which cement pastes were prepared with and without the replacement of nano-silica, and the effect of nano-silica was examined using various techniques, including XRD, SEM, and TGA.

1.1 Research significance

As discussed earlier, nano-silica is a superior SCM, and its early strength gain is of interest. However, an optimal dosage is required to ensure the effectiveness of other cementitious materials. Otherwise, its effectiveness is hindered by overdosage, owing to agglomeration. Determining the optimal dosage for a specific purpose is laborious and time-consuming. Therefore, this study proposes an integrated cement hydration and thermodynamic model to assess the effect of replacing nano-silica in cement paste in terms of phase assemblages, and a microscale finite element scheme to evaluate the nonlinear behaviour of nano-silica reinforced cement paste during the hydration stage. Notably, the proposed model, initiated with the chemical and physical properties and curing conditions of cementitious materials (cement and nano-silica), continually predicted the intrinsic mechanical properties until the required hydration age. The proposed model was further validated with experimental results, which were comparable. Thus, the proposed model can be further developed to predict the mechanical

properties of nano-silica-modified mortar and concrete, making it a tool for material optimisation and performance prediction of cement-based materials.

2. Experimental procedures

2.1 Materials and sample preparation

Ordinary Portland cement (OPC), which conforms to the Japan Industrial Standard JIS R 5201:2015, was acquired from the Japan Cement Association. Nano-silica, with an average particle size of 18.5 nm and 99.9% purity, was purchased from Kanto Chemical. Co., Inc. The XRD pattern in **Fig. 1** confirms the amorphous phase of the nano-silica. The chemical and physical properties of the cement and nano-silica are listed in **Table 1.**

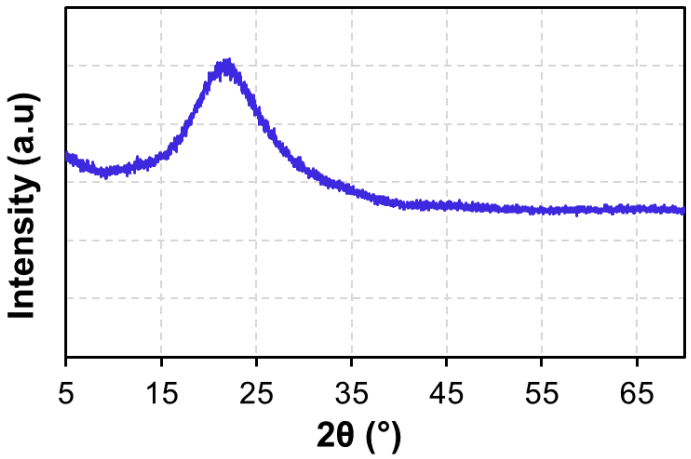

Fig. 1. XRD pattern verifying the amorphous phase of nano-silica.

145 **Table 1**. Chemical composition and physical characteristics of utilised cement and nano-silica
146 (wt. %)

Properties	**Cement**	**Nano-Silica**
SiO_2	21.42	>99.5
Al_2O	5.52	-
Fe_2O_3	2.81	-
CaO	64.23	-
MgO	1.42	-
SO_3	2.17	-
Na_2O	0.25	-
K_2O	0.58	-
TiO_2	0.27	-
P_2O_5	0.42	-
MnO	0.04	-
Cl	0.015	-
Density (kg/m^3)	3160	2200
Specific surface area (m^2/kg)	339	33700

147
148
149 Nano-silica was incorporated into cement pastes at replacement levels of 0, 2, and 4% by weight,
150 while maintaining a consistent water-binder ratio of 0.40 across all mixtures. The workability of each
151 mixture was evaluated by measuring the flow diameter at intervals of 0, 20, 60, and 120 min as
152 outlined in JASS15M-103. **Fig. 2** illustrates a substantial decrease in slump compared to the control
153 sample, with flow reductions of 33.9 and 38.1% observed for the 2 and 4% replacement levels,
154 respectively, at the initial stage (zero minutes). This decrease in workability associated with nano-
155 silica incorporation was attributed to its high water retention capacity [29], stemming from its high

surface area and reactivity. This characteristic reduces the amount of free water necessary for fluidity in the mixture, thereby increasing viscosity and resulting in decreased workability. Previous research has revealed similar findings with nanoparticles possessing high surface areas [8,30]. The water demand associated with the incorporation nano-silica in cement pastes can be effectively managed by introducing appropriate quantities of superplasticisers to achieve the desired workability [31]. Notably, this study did not use superplasticisers, as it falls beyond the scope of the present investigation. The compositions of the mixtures are listed in **Table 2**.

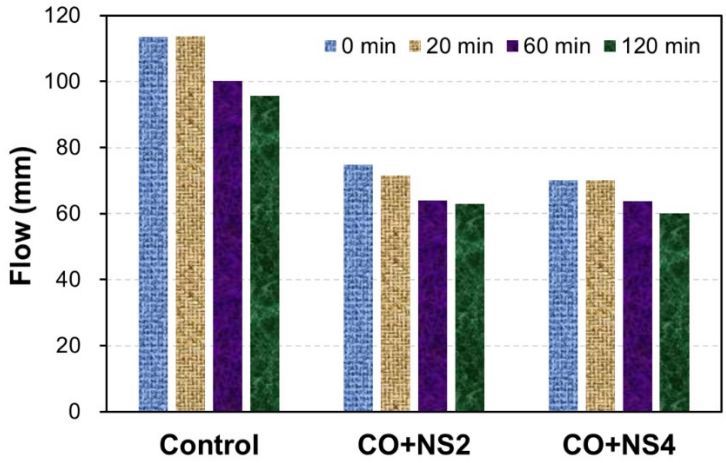

Fig. 2. Changes of flow with time for all the pastes

Table 2. Composition of the paste mixtures

Sample ID	Cement (g)	Nano-silica (g)	Water (g)
CO	100	0	40
CO+NS2	98	2	40
CO+NS4	96	4	40

Owing to the ultrafine nature of nano-silica particles and their strong van der Waals forces [32], which can result in particle agglomeration, a specified quantity of deionised water and nano-silica were combined in a beaker. The resulting mixture was ultrasonically dispersed for 10 min. The dispersed

172 solution was subsequently introduced into a cement blend using a Hobart N50 5-Quart mixer. The
173 mixing process involved an initial one-minute period at low speed, followed by another one-minute
174 at high speed. After pausing the mixing, the surface of the bowl was cleared using a spatula, following
175 which a two-minute high-speed mixing implemented to ensure the uniformity of the pastes. The
176 prepared pastes were poured into lightweight cylindrical moulds measuring with a diameter and
177 height of 50 and 100 mm, respectively, in a two-layer arrangement. Each layer was subjected to 20 s
178 of vibration to eliminate larger pores, which may have arisen due to reduced workability. Once
179 moulded, the specimens were hermetically sealed and placed in a curing environment at a constant
180 temperature of 20 ± 2°C. After a curing period of 24 hours, the specimens were carefully removed
181 from the moulds, covered in polyester film, and stored under controlled conditions at 20 ± 2°C. The
182 specimens of designated ages (1, 3, 7, 28, and 56 d) were finely crushed into pieces measuring 20
183 mm or less using a hammer [33]. Subsequently, they were immersed in acetone for three days to halt
184 the hydration process. The specimen pieces were separated using suction filtration and placed in a
185 temperature chamber set at 40°C for two days to eliminate residual acetone. Once thoroughly dried,
186 the samples were carefully ground using a mortar and pestle to avoid excessive heating. The resulting
187 powder was sifted through a 75 μm sieve for subsequent measurements.
188
189 **2.2 Experimental Characterisation**
190 The effectiveness of nano-silica in enhancing the strength was evaluated using an automatic
191 compressive strength testing machine (Hi-ACTIS-2000), following the ISO 679 standard. A constant
192 load rate of 0.6 $N/mm^2 \cdot s$ was maintained, with three replicate specimens per hydration age (1, 3, 7,
193 28, and 56 days) to ensure reliable compressive strength measurements. Cement hydration with and
194 without nano-silica was quantified by TGA under a nitrogen atmosphere, using a HITACHI TG/DTA
195 7220 instrument. The heating rate was 10 ºC/min within a temperature range of 20–950ºC.
196 Furthermore, a Rigaku X-ray diffractometer, utilising CuKα radiation and adhering to the following
197 conditions, was employed to determine the hydrate contents: a tube voltage of 40 kV, tube current of

40 mA, scanning range (2θ) of ~5–70°, step width of 0.02°, and scanning speed of 6.5 °/min. A BGMN Rietveld refinement program (Profex) was used for phase quantification. The morphologies of the hydrates and their elemental compositions were studied by SEM and energy-dispersive X-ray spectroscopy (EDS). The powdered samples were coated with a thin gold layer before examination using a JSM-IT200 microscope (JEOL, Japan), operated at 15 kV and a working distance of 10 mm.

3. Modelling approach

3.1 Coupled hydration and thermodynamic model

Thermodynamic models have emerged as valuable tools for understanding the intricate chemical reactions occurring during cement hydration [34,35]. By employing thermodynamic principles, these models facilitate the prediction of phase assemblages, hydration products, and properties of cementitious systems [36]. In this study, chemical thermodynamic calculations of the phases formed during hydration were conducted using the open-source geochemical software PHREEQC [37]. The phases considered in this study were consistent with those employed in [36], ensuring continuity and comparability. However, additional consideration was given to the equilibrium of various calcium–silicate–hydrate (C-S-H) phases as end members in the chemical thermodynamic calculations [38]. This consideration is crucial because of the influence of nano-silica in altering the formation of C-S-H phases by modifying the Ca/Si ratio [39–41]. The phase equilibrium module, which relies on the mass-action equation [37], was utilised to predict the stable solid phases and pore solution composition in the hydrated cement matrix with respect to hydration time, based on thermodynamic principles [35]. Essential parameters, such as equilibrium constants (log Kp) and standard heats of reaction (ΔrH_0), were obtained from Cemdata18 [38] and the default database within the PHREEQC software. The phase equilibrium module utilised in this study requires specific input parameters, including a designated saturation index (set at zero for equilibrium) and the quantity of each phase. To quantify the amounts of the major clinker phases, such as C_3S, C_2S, C_3A, and C_4AF, at each time

224 step, a cement hydration model developed by Parrot and Killoh [42] was employed. The Parrot–
225 Killoh model has been extensively employed and validated through experimental findings from
226 various prior studies [35,43]. Their approach encompasses three main controlling mechanisms for a
227 realistic consideration of the reaction degree of each clinker phase: nucleation and growth of products
228 (Eq. (1)), diffusion of ions through the layers of previously formed products (Eq. (2)), and formation
229 of hydrate shells around the unreacted material (Eq. (3)). These mechanisms are described by Eqs.
230 (1–3). Among these three reaction rates ($R_{t,1}^m$, $R_{t,2}^m$, and $R_{t,3}^m$), the minimum value is chosen as the
231 actual controlling rate for calculating the hydration degree α_t^m at time t using Eq. (4).
232
233 Nucleation and growth rate ($R_{t,1}^m$):

234 $$R_{t,1}^m = \frac{K_1}{N_1}(1-\alpha_t^m)(-\ln(1-\alpha_t^m))^{(1-N_1)} \quad (1)$$

235 Diffusion rate ($R_{t,2}^m$):

236 $$R_{t,2}^m = \frac{K_2(1-\alpha_t^m)^{(\frac{2}{3})}}{1-(1-\alpha_t^m)^{(\frac{1}{3})}} \quad (2)$$

237 Hydrates shell formation ($R_{t,3}^m$):

238 $$R_{t,3}^m = K_3(1-\alpha_t^m)^{N_3} \quad (3)$$

239 The hydration degree of a clinker mineral (α_t^m):

240 $$\alpha_t^m = \alpha_{t-1}^m + \Delta t \cdot \min(R_{t,1}^m, R_{t,2}^m, R_{t,3}^m) \cdot \beta w_{/c} \cdot \lambda_{RH} \cdot \frac{A}{A_0} \cdot \exp\left(\frac{E_a^m}{R}\left(\frac{1}{T_0}-\frac{1}{T}\right)\right) \quad (4)$$

241 Here,

242 $$\beta w_{/c} = (1 + 3.333 \cdot \left(H^m \cdot \frac{w}{c} - \alpha_{t-1}\right))^4 \qquad for\ \alpha_{t-1} > H^m \cdot \frac{w}{c} \quad (5)$$

243 $$\beta w_{/c} = 1 \qquad for\ \alpha_{t-1} \leq H^m \cdot \frac{w}{c} \quad (6)$$

244 $$\lambda_{RH} = \left(\frac{RH-0.55}{0.45}\right)^4 \quad (7)$$

245

In the above equations, T represents the actual curing temperature in K, T_0 corresponds to a reference temperature (293.15 K), Δt denotes the time interval, $\frac{w}{c}$ stands for the water-to-cement ratio, RH signifies the relative humidity, A represents the Blaine surface area of the cement (m^2/kg), A_0 is the reference surface area of cement (385 m^2/kg), E_a^m is the apparent activation energy of the clinker mineral, and K_1, N_1, K_2, K_3, N_3, and H are equation constants associated with the type of clinker mineral. The specific values used for OPC are listed in **Table 3.**

Table 3. Coefficients for computing the hydration degree of the clinker phases [44,45]

	C_3S	C_2S	C_3A	C_4AF
K_1	1.5	0.5	1	0.37
N_1	0.7	1	0.85	0.7
K_2	0.05	0.006	0.04	0.015
K_3	1.1	0.2	1	0.4
N_3	3.3	5	3.2	3.7
H	1.8	1.35	1.6	1.45
E_a (J/mol)	41,570	20,785	54,040	34,087

Based on the estimated hydration degree of individual clinker phases (α_{C_3S}, α_{C_2S}, α_{C_3A}, and α_{C_4AF}), the overall hydration degree of cement paste (α_c) for a given time step can be calculated as outlined in Eq. (8).

$$\alpha_c = \frac{\alpha_{C_3S}.W_{C_3S} + \alpha_{C_2S}.W_{C_2S} + \alpha_{C_3A}.W_{C_3A} + \alpha_{C_4AF}.W_{C_4AF}}{W_{C_3S} + W_{C_2S} + W_{C_3A} + W_{C_4AF}} \quad (8)$$

Here, W_{C_3S}, W_{C_2S}, W_{C_3A}, and W_{C_4AF} represent the mass fractions of the individual clinker phases.

Upon mixing cement with water, K, Na, and S ions are released into the pore solution because of the dissolution of soluble alkali sulphates, and less soluble minerals, such as gypsum and calcite, partially dissolve until an equilibrium with the pore solution is attained. In this context, gradually dissolving clinker phases was assumed to continuously release Ca, Si, Al, Fe, and hydroxide ions in proportion to the degree of reaction of the individual phases. Meanwhile, minor components in the cement matrix like Na_2O, K_2O, and MgO release Na, K, Mg, and O ions into the pore solution as a function of the total hydration degree (α_c) for a specific time.

Furthermore, the degree of nano-silica was determined based on the pozzolanic reaction between portlandite and nano-silica, as proposed in a previous study [46] and depicted in Eq. (9). It is evident that the reaction degree of nano-silica primarily depended on the availability of portlandite (CH), which is a by-product of the hydration of the C_3S and C_2S phases, at every time step. Stoichiometric calculations based on Eqs. (9) revealed that 0.74 g of nano-silica reacts with 1 g of portlandite during the pozzolanic reaction. Additionally, the formation of portlandite due to hydration decreased as the replacement ratio of nano-silica increased. By considering these factors, the proposed equation (Eq. (10)) accurately describes the degree of nano-silica.

$$1.1CH + S + 2.8H \rightarrow C_{1.1}SH_{3.9} \quad (9)$$

$$\alpha_s(t) = \frac{\mu\left(W_{C_3S}\times 0.49\times\alpha_{C_3S}(t) + W_{C_2S}\times 0.22\times\alpha_{C_2S}(t)\right)\times 0.74}{W_s/W_c} \quad (10)$$

Here, α_s is the degree of pozzolanic reaction, and μ (a constant) is the ratio of reacted silica to the total amount of nano-silica added. The value was taken as 0.05 by calibrating the experimental results [47] of the cement paste at a particular degree of hydration.

W_{C_3S} and W_{C_2S} are weight ratio of the C_3S and C_2S phases in the cement, respectively.

$\alpha_{C_3S}(t)$ and $\alpha_{C_2S}(t)$ are the reaction degrees of the C_3S and C_2S phases, respectively.

W_s and W_c are total weight of nano-silica and cement, respectively, in the mix.

The aforementioned (hydration and thermodynamic) models were coupled and simulated to predict the solid assemblage of the hydration products and dissolution of clinker minerals over hydration time, as shown in **Fig. 3**. A small time step was used, particularly during the early stages of hydration, to accurately capture the rapid changes. The time step was then gradually adjusted as the hydration progressed to stabilise the simulation.

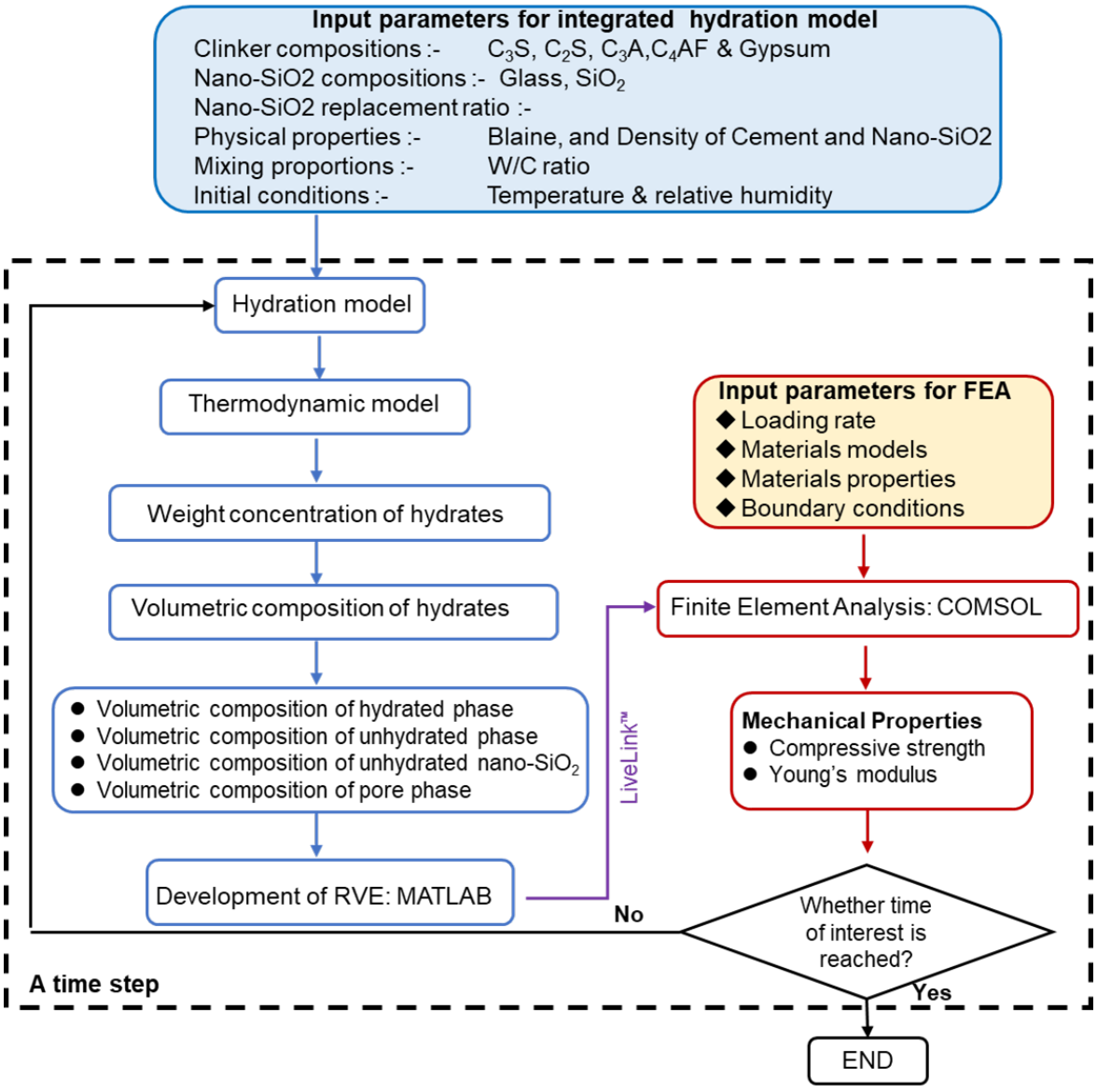

Fig. 3. Schematic illustration of the proposed model.

3.2 Volume fraction of hydrates

In this study, the total weight of the C–S–H matrix, as predicted by the coupled model mentioned above, was further categorised into two distinct components, namely low- and high-density C-S-H, for the accurate prediction of hydrate assemblages using the correlation in Eq. (11), as suggested by Tennis and Jennings [48]. This categorisation follows the research conducted by Constantinides and Ulm [49], who observed the development of C–S–H primarily on the surface of the cement particles during the early stages of the hydration process. However, as time progressed, the cement particles became partially or fully covered by a layer of C–S–H, and further growth of C–S–H occurred within the confined spaces as a result of the diffusion of clinker minerals such as C_3S and C_2S. Consequently, the outer layer of C–S–H formed on the surface exhibited a lower density than the inner C–S–H, which grew within confined spaces. The average densities of the high-density (HD) and low-density (LD) C-S-H were obtained from the literature. Without the incorporation of nano-silica, the densities were 2000 and 1700 kg/m^3, respectively [48]. With the incorporation of nano-silica, the densities changed to 1800 and 1500 kg/m^3, respectively, owing to the transformation of C-S-H from a jennite-like structure to a tobermorite structure [50].

$$M_r = 3.017\,(w/c)\alpha - 1.347\alpha + 0.538 \quad (11)$$

In addition, it is essential to consider the molar volume differences between the hydration products and clinker minerals. This difference leads to a phenomenon known as chemical shrinkage, where the total volume of the hydration products is less than the total volume of the clinker minerals; this phenomenon contributes to self-desiccation and autogenous contraction in cementitious systems [51,52]. Previous studies have often overlooked or assumed constant percentages of reacted cement; however, this can have implications in accurately predicting capillary porosity. The total chemical shrinkage was calculated by multiplying the weight proportion of each phase by its corresponding shrinkage coefficient [53].

The volumes of the hydration products were determined based on their respective molar volumes. Subsequently, the capillary porosity of the cement matrix was estimated using an equilibrium approach by calculating the difference between the initial and final volumes of the hydration products. This calculation considers factors such as chemical shrinkage and unreacted clinker minerals, as shown in Eqs. (12). The evaluation of the chemical shrinkage involved multiplying the reacted clinker phases with their respective shrinkage coefficients, which were 0.0704 for C_3S, 0.0724 for C_2S, 0.171 for C_3A (when converting to ettringite), 0.115 for C_3A (when converting to monosulfoaluminate), 0.117 for C_4AF (when converting to ettringite), and 0.086 for C_4AF (when converting to monosulfoaluminate) [54].

$$V_{cap} = V_i - (V_{UC} + V_{HP} + V_{CS}), \quad (12)$$

where V_{cap} is the volume of the capillary pore space, V_{CS} is the chemical shrinkage, V_i is the initial volume of the matrix, V_{UC} is the unreacted clinker volume, and V_{HP} is the volume of the hydration products.

3.3 Development of representative volume elements for paste

Simulating the actual microstructure of cement paste using the current advanced computing technologies presents significant challenges in terms of computational time. This is primarily due to the presence of nanoscale gel pores, which typically range from 0.5 to 10 nm in size [55]. Incorporating these nanoscale phases into a microscale model introduces computationally demanding complexity. Nevertheless, researchers have successfully employed simplified microstructural models to analyse the mechanical properties of cement pastes [56,57]. However, owing to the significant computational requirements for simulating a numerically generated three-dimensional (3D) cement specimen, the 3D model was successfully converted into an equivalent two-dimensional (2D) plane

element using probabilistic and statistical approaches [58,59]. Although this 2D representation ignores out-of-plane factors, several earlier studies [60–62] have shown that using a comparable 2D model has a minor impact on homogenised mechanical responses compared to a full 3D model.

Hence, we developed a 2D representative volume element in MATLAB based on the predicted volume fractions in Section 3.2. To preserve the heterogeneity of the cement paste, the matrix material was assumed to represent the hydrated phase, while the unhydrated cement, unreacted nano-silica, and pore phases were randomly dispersed [61,63]. The volume fraction of the unhydrated phase within the representative volume element was determined by adding the volumes of the major clinker phases (C_3S, C_2S, C_3A, and C_4AF) at each time step, as described in Section 3.2. Conversely, the pore phase was calculated by combining the capillary pore volume and chemical shrinkage at each time step. Moreover, the unhydrated cement, unreacted nano-silica particles, and pores were represented by independent circular particles and circular cavities, following approaches found in the literature [61,64,65]. The "take-and-place" method was utilised to ensure the random distribution and non-overlapping arrangement of the particles [58,59]. To maintain consistency with the actual hydration process and microstructural development, the sizes of the particles representing the unhydrated phase were determined as a function of the degree of hydration by maintaining the area/volume ratio at any hydration time, as described by Eqs. (13).

$$R_t = R_i(1 - \alpha_c)^{1/3}, \tag{13}$$

where R_t, R_i, and α_c are the radii of a particle at time *t*, initial radii of the particle, and degree of cement hydration, respectively.

The clinker particles and pores in cement paste exhibit a wide range of sizes, from nanometres to several micrometres. However, including the actual particle distribution in the numerical analysis introduces computational complexity. The grain sizes of cement particles typically fall within the

range of 7–200 μm [66], and 50% of the cement particles pass through a size of 15 μm [67]. Subsequently, the initial size of the anhydrous particles was set at 15 μm. In addition, capillary pores in cement paste have been reported to range in size from 10 nm to 100 μm, with a peak distribution between 4–6 μm [27]. Accordingly, two pore sizes (6 and 4 μm) were considered, each contributing 50% to the total pore volume, unlike other studies that considered mono-sized pores [61,63].

Moreover, previous studies have proposed various approaches to represent significantly more minor inclusions, such as unreacted nano-silica particles, compared to the size of the RVE. Maekawa et al. [27] suggested using the equivalent radius calculated from the geometric mean to account for the different orders of magnitude of the pore radii in concrete modelling. Rupasinghe et al. [63] employed lumping techniques to represent nanoparticles smaller than 10 nm at the micro-level by aggregating smaller individual particles. These particles were approximately 10^4 times smaller than the 100 μm-sized RVE. Therefore, this study adopted mono-size particles, whose size was set to 4 μm, to represent unreacted nano-silica particles in cement paste. Similar approaches that consider the pores within a given RVE at the concrete mesoscale can be found in [68].

To ensure numerical accuracy and computational efficiency when predicting material properties using a sequential homogenisation approach in a multiscale model [69], selecting an appropriate size for the RVE is crucial. Previous studies have indicated that reliable predictions of the mechanical characteristics of cement paste can be achieved using RVE sizes ranging from 100 μm to 200 μm [70]. Therefore, a representative volume element size of 100 μm was chosen for modelling cement paste in this study. **Fig. 4** illustrates the geometry of the RVE developed based on the selected values for unhydrated cement particles, pores, and the 100 μm RVE size, corresponding to seven-day aged cement pastes with a water-cement ratio of 0.4.

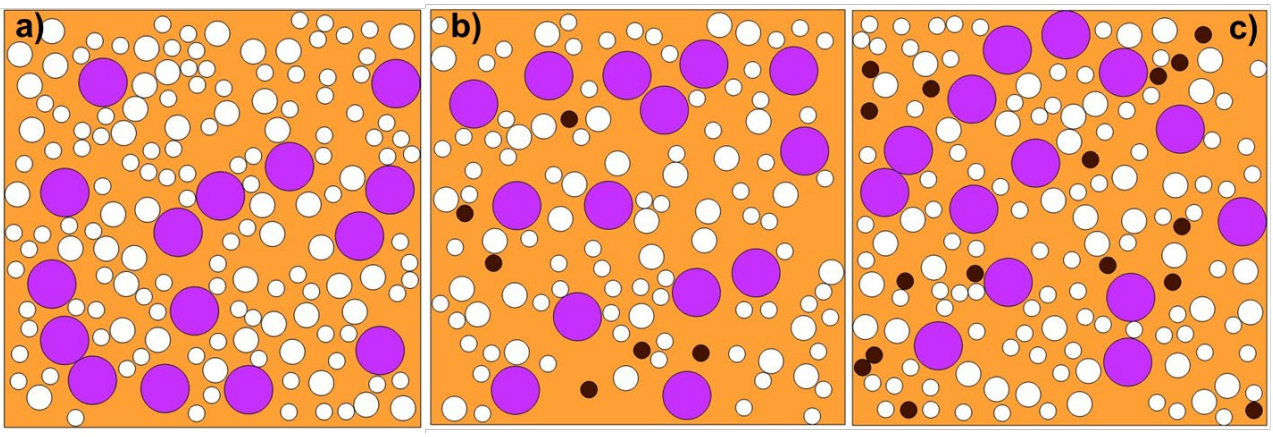

Fig. 4. Geometry of the RVE of seven-day aged cement pastes: (a) CO, (b) CO+NS2, and (c) CO+NS4 (Orange, magenta, black, and white colours represent the hydrated phase, unhydrated cement particles, unreacted nano-silica particles, and pores, respectively).

3.4 Numerical investigation of the RVE

3.4.1 Materials modelling, loading conditions, and boundary constraints

The finite element analysis of the RVE for cement pastes, developed in Section 3.3, was performed using the structural mechanics module in COMSOL Multiphysics 6.0 [71]. As shown in **Fig. 4**, the RVE generated in MATLAB is transferred to COMSOL using the LiveLink of the MATLAB tool [72]. To determine the homogenised mechanical properties of the cement paste, the material behaviour of each phase was defined using COMSOL. In a previous study by Rupasinghe et al. [63], hydrated products and unhydrated clinkers were modelled as linearly elastic perfectly plastic materials, and it was demonstrated that these simplifications had a negligible influence on the homogenised elastic modulus and strength. However, considering the nonlinear behaviour of cementitious materials, this study employs the Bresler–Pister yield criterion proposed by Bresler and Pister [73]. The Bresler–Pister yield criterion is a constitutive model developed specifically to assess the strength of concrete subjected to multiaxial stress. This yield criterion represents an extension of the well-known Drucker–Prager criterion to account for the brittle behaviour of concrete. The Bresler–Pister yield criterion is expressed in terms of stress invariants, as shown in Eq. (14). Although

this material is commonly utilised to simulate concrete components, to the best of our knowledge, its utilisation in multiscale methodologies for nanocomposites of cement paste has not been documented.

$$F_y = \sqrt{J_2} + k_1 I_1^2 + k_2 I_1 + k_3 \quad (14)$$

Here, k_1, k_2, and k_3 are the function of the uniaxial compressive strength (σ_{cs}), uniaxial tensile strength (σ_{ts}), and biaxial compressive strength (σ_{bc}), and their detailed description can be found in [71].

In contrast, the unhydrated clinkers exhibited a much higher strength than the hydrated products. For instance, the tensile strength of unhydrated cement reported in several studies was 683 MPa [56,74], whereas those of the hydrated products were 58–92 MPa. These values were obtained through inverse analysis of the experimental results and nanoindentation techniques [75]. Therefore, to account for the higher stiffness and strength, this study modelled unhydrated clinkers as linearly elastic materials [74,76]. Similarly, the unreacted nano-silica particles were modelled as linear elastic materials.

To simulate the uniaxial compressive test, the bottom surface of the RVE was immobilised to restrict movement along the y-direction, as illustrated in **Fig. 5**. A prescribed displacement was applied to the top surface in the negative y-direction to simulate compressive loading. Furthermore, the bottom-left corner of the RVE was restrained horizontally to prevent rigid-body motion in the horizontal direction. Additionally, periodic boundary conditions were implemented on opposite vertical surfaces to simulate infinite repetition within a limited computational domain.

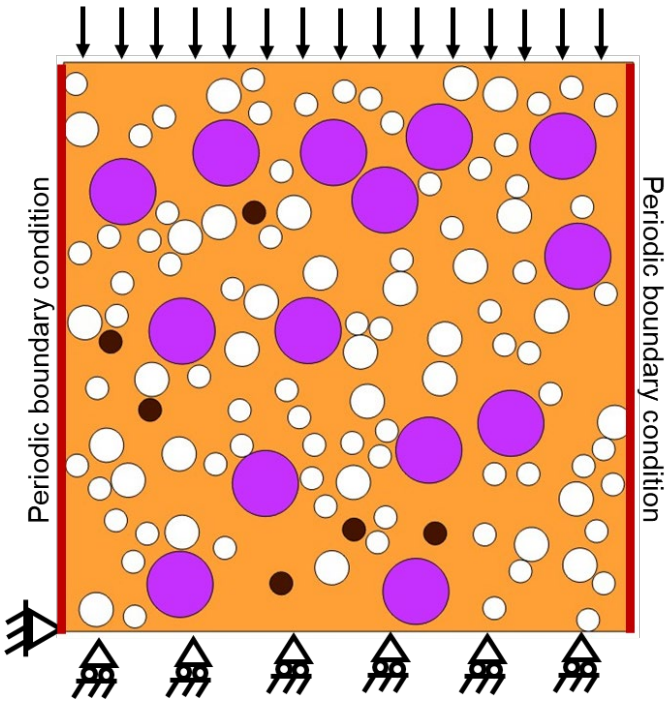

Fig. 5. Boundary conditions applied on the RVE.

3.4.2 Input parameters for material models

The Bresler–Pister yield criterion adopted to model the mechanical behaviour of the hydrated phase requires specific input parameters, such as Young's modulus, Poisson's ratio, density, tensile strength, compressive strength, and biaxial compressive strength. In this study, a Poisson's ratio of 0.24 was assigned to the hydrated phase [77], while the remaining input parameters were allowed to vary with hydration time to capture the evolving properties of the cement matrix as the microstructure developed. Unlike previous studies [63,78], the contributions of hydrates, such as C-S-H, ettringite, monosulfate, and portlandite, in strengthening of the hydrated phase were also considered. Consequently, the effective parameters of the hydrated phase were calculated using Eqs. (15), as outlined in a previous study [79]. The intrinsic mechanical properties of the individual phases are summarised in **Table 4**.

$$X_t^m = \sum (VF)_t^m \times Y_t^m \quad (15)$$

458 Here, X represents the effective properties, such as the compressive strength, Young's modulus, and
459 density of the hydrated phase at a particular hydration time.
460 VF is the volume fraction of the m^{th} phase (where m corresponds to C-S-H (LD and HD), portlandite,
461 ettringite, or monosulfate) in the hydrated phase at a particular time.
462 Y represents intrinsic properties, such as compressive strength, Young's modulus, and density of the
463 m^{th} phase (C-S-H, ettringite, monosulfate, or portlandite) at a particular hydration time.
464
465 Furthermore, in this study, the effective compressive strength of the hydrated phase was attributed
466 solely to the compressive strength of the C-S-H phase. This is because experimental data for other
467 phases were unavailable, Furthermore, previous studies, such as that by Tailor [80], indicated that the
468 C-S-H matrix predominantly contributes to the overall strength of the hydrated matrix. In addition,
469 owing to the lack of experimental results for the tensile and biaxial strengths of the hydrated phase,
470 assumptions were made based on the Griffith model [81], which describes the failure and damage
471 mechanics of cement-based materials. Consequently, the tensile strength of the hydrated phase was
472 assumed to be 1/8 times the compressive strength of the C-S-H matrix, and the biaxial strength was
473 1.2 times the strength of the C-S-H matrix.
474
475 **Table 4.** Mechanical properties of hydrates

Phases/properties	Young's modulus (GPa)	Compressive strength (MPa)	Density (kg/m3)	Ref.
C-S-H (LD)	21.7	528	1700/1400*	[74]
C-S-H (HD)	29.4	856	2000/1700*	[74]
Portlandite	38	-	2240	[67]
Ettringite	22.4	-	1800	[82]
Monosulfate	38	-	1990	[67]

476 *When nano-silica is incorporated

The input parameters for the unhydrated phase were Young's modulus, Poisson's ratio, and density. The density of the unhydrated phase was based on the actual density of the clinker, which was used as input for the coupled model (Section 3.1). The Young's modulus and Poisson's ratio were assumed to be constant at 137 GPa and 0.3, respectively. These values were selected because the material properties of the clinker remained constant during hydration. Additionally, these values are consistent with the findings reported in literature [63,77]. Similarly, Young's modulus, Poisson's ratio, and density of unreacted nano-silica were assumed to be 70 GPa, 0.21, and 2200 kg/m³, respectively. These values, selected based on similar studies [83], provide a reasonable representation of the material properties. Furthermore, circular voids were incorporated into the pore phase within the hydrated phase.

3.4.3 Finite element analysis and homogenised mechanical properties

The RVEs were meshed using triangular plane elements. Capillary pores were not meshed but instead regarded as cavities embedded within the hydrated phase. The homogenised microscopic stress was determined by averaging the stress tensor (σ_y) and field across the RVE domain, as shown in Eq. (16). Similarly, the homogenised microscopic strain was computed by averaging the strain tensor (ε_y) over the RVE domain (Eq. (16)).

$$\bar{\sigma}: \bar{\varepsilon} = \frac{1}{|A|} \int_R \sigma_y : \varepsilon_y \, dy \tag{16}$$

Subsequently, a stress-strain curve was generated, and important homogenised material properties, including the compressive strength and Young's modulus, were determined. The maximum stress value on the curve was taken as the compressive strength of the material, whereas the initial slope of the stress-strain curve was the Young's modulus.

4. Results and discussions

4.1 Analysis of hydration products

4.1.1 Thermogravimetric analysis

TGA was performed on all the cement pastes (CO, NS2, and NS4) at different hydration ages (1, 3, 7, 28, and 56 days). Differential thermogravimetry curve (DTG) and mass losses are plotted in **Fig. 6**. These DTG profiles consistently exhibited two distinct peaks at all hydration ages, indicative of the release of unbound and bound water from the phases encompassing C-S-H, ettringite, and monosulfate within the temperature range of 80–200°C [63], and of portlandite (CH) decomposition around 450°C [13]. Subsequently, the CH content was quantified using Eq. (17).

$$CH = (WL)_{CH} \cdot \frac{74}{18}, \quad (17)$$

where $(WL)_{CH}$ is the weight loss due to the decomposition of portlandite in the TG curve, and the fraction (74/18) is the ratio of the molar masses of portlandite (CH) and water (H_2O).

Fig. 6 shows how the introduction of nano-silica led to an increased CH content during the initial stages, specifically on days 1 and 3. This enhancement can be attributed to the nucleation effect of nano-silica, which accelerates cement hydration and consequently boosts the CH production [39]. This effect was most pronounced at a 2% replacement level. However, after three days, the CH content declined owing to the pozzolanic effect, where CH was consumed, leading to reduced free CH content within the cement matrix [5]. Furthermore, to account for the dilution effect resulting from the decreased cement content in the mixture due to the incorporation of nano-silica, the CH contents across all formulations were normalised to the nano-silica substitution level. These normalised values were then plotted against the hydration age, as shown in **Fig. 7**. **Fig. 7** distinctly illustrates the CO+NS4 sample, exhibiting a reduced CH content at all ages. This can be attributed to the dominant influence of the pozzolanic effect on the nucleation effect at higher replacement levels

529 [4,20]. Additionally, the aggregation effect of nano-silica, owing to its substantial surface area, may
530 hinder the hydration process, thereby highlighting this reduction. This observation is further
531 supported by **Fig. 6**d, which shows significant decomposition of C-S-H. The tendency for aggregation
532 could potentially limit the reactivity and hinder the diffusion of clinker minerals, consequently
533 affecting the overall CH production during hydration [84]. Notably, certain studies [41,63] have
534 presented conflicting findings, indicating a reduction in CH content upon the introduction nano-silica
535 during the initial stages of hydration. However, these investigations did not distinctly explain the
536 effects of the nucleation sites and pozzolanic reactions [63,79]. In contrast, the results of the present
537 study clarify the actual influence of nano-silica on cement paste hydration [85]. These observations
538 suggest that the existence of an optimal level of cement replacement with nano-silica. Below this
539 optimal threshold, free calcium hydroxide (CH) remains in the mixture, and the quantity of nano-
540 silica within the paste is insufficient to fully react with CH. Conversely, surpassing the optimal nano-
541 silica content results in a lack of available CH for interaction with nano-silica, causing the
542 nanoparticles to primarily function as inert fillers without actively participating in the pozzolanic
543 reactions. Considering the specific experimental parameters and type of nano-silica employed, the
544 analysis conducted in this study clearly advocates a 2% replacement level of nano-silica as the optimal
545 configuration to achieve maximum benefits through nucleation and pozzolanic reactivity.

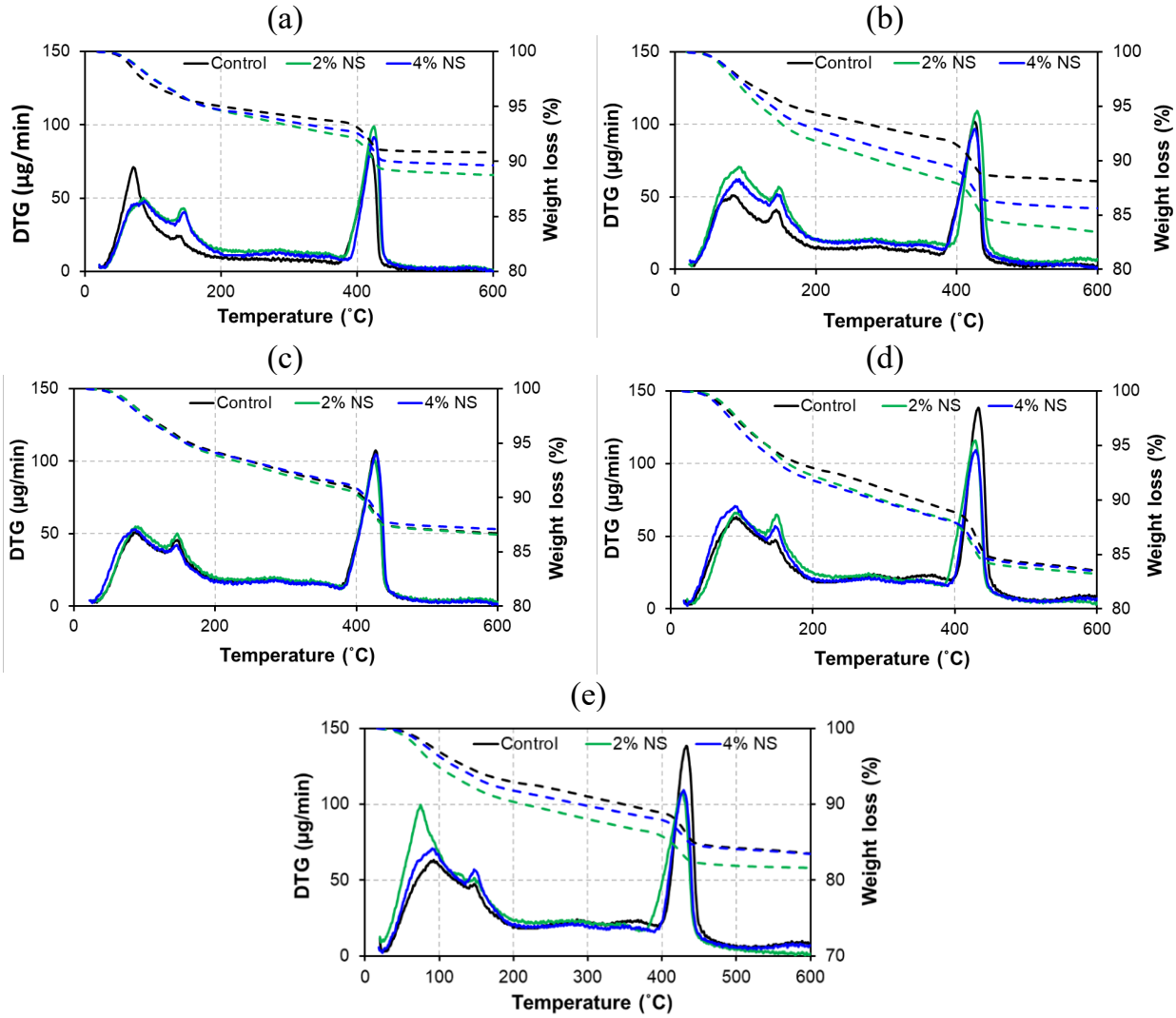

Fig. 6. TGA and DTA curves of the cement pastes at (a) one, (b) three, (c) seven, (d) 28, and (e) 56 days.

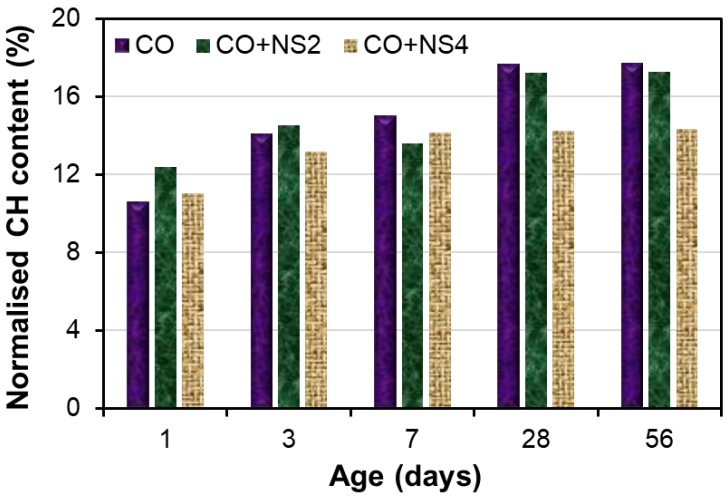

Fig. 7. Normalised CH content of the cement pastes at different ages.

552 **4.1.2 Analysis of the XRD diffraction patterns of cement pastes**

553 **Fig. 8** depicts the X-ray diffraction patterns for all the paste samples (CO, CO + NS2, and CO + NS4)
554 at different hydration ages (1, 3, 7, 28, and 56 days). As shown in **Fig. 8**, portlandite, ettringite,
555 monosulfate, alite, and belite are the principal crystalline phases at all hydration ages. Notably, the
556 peak intensities associated with these phases exhibited distinct variations upon nano-silica
557 substitution. Fig. **8**(a) highlights that the presence of nano-silica leads to increased intensity
558 corresponding to ettringite (2θ = 9.1) and monosulfate (2θ = 9.9). This increase confirms the
559 acceleration of cement hydration induced by nano-silica. Conversely, the peak intensity attributed to
560 portlandite (2θ = 34.1) diminished upon the introduction of nano-silica. This reduction is aligned with
561 the increased pozzolanic activity of nano-silica, which engages in the substantial consumption of
562 portlandite, thereby fostering the generation of supplementary C-S-H [63]. Compared to the earlier
563 stages, this trend was particularly noticeable at days 7, 28, and 56, supporting the findings discussed
564 in Section 4.1.1. These observations collectively enabled a qualitative analysis of the influence of
565 nano-silica on cement clinker through variations in the peak intensity. **Fig. 9** provides a graphical
566 representation of the hydration reactions within individual clinker minerals (C_3S, C_2S, C_3A, and
567 C_4AF) and overall degree of cement hydration, as determined by the XRD/Rietveld analysis.
568 Although the hydration degree of C_3A remained unchanged, the presence of nano-silica significantly
569 affected the hydration degrees of C_3S, C_2S, and C_4AF. This effect can be attributed to the apparent
570 pozzolanic reactivity and nucleation effect caused by nano-silica. However, these alterations in the
571 degree of hydration did not affect the overall degree of cement hydration (**Fig. 9**(e)). Furthermore, a
572 comparison of the predicted hydration reactions of the clinker minerals (using the coupled hydration
573 and thermodynamic model outlined in Section 3.1) with the experimental values over the hydration
574 age is presented in **Fig. 9**. This comparison illustrates the remarkable reliability of the coupled models
575 in accurately reproducing the realistic evolution of the clinker mineral reactions over the hydration
576 age.
577

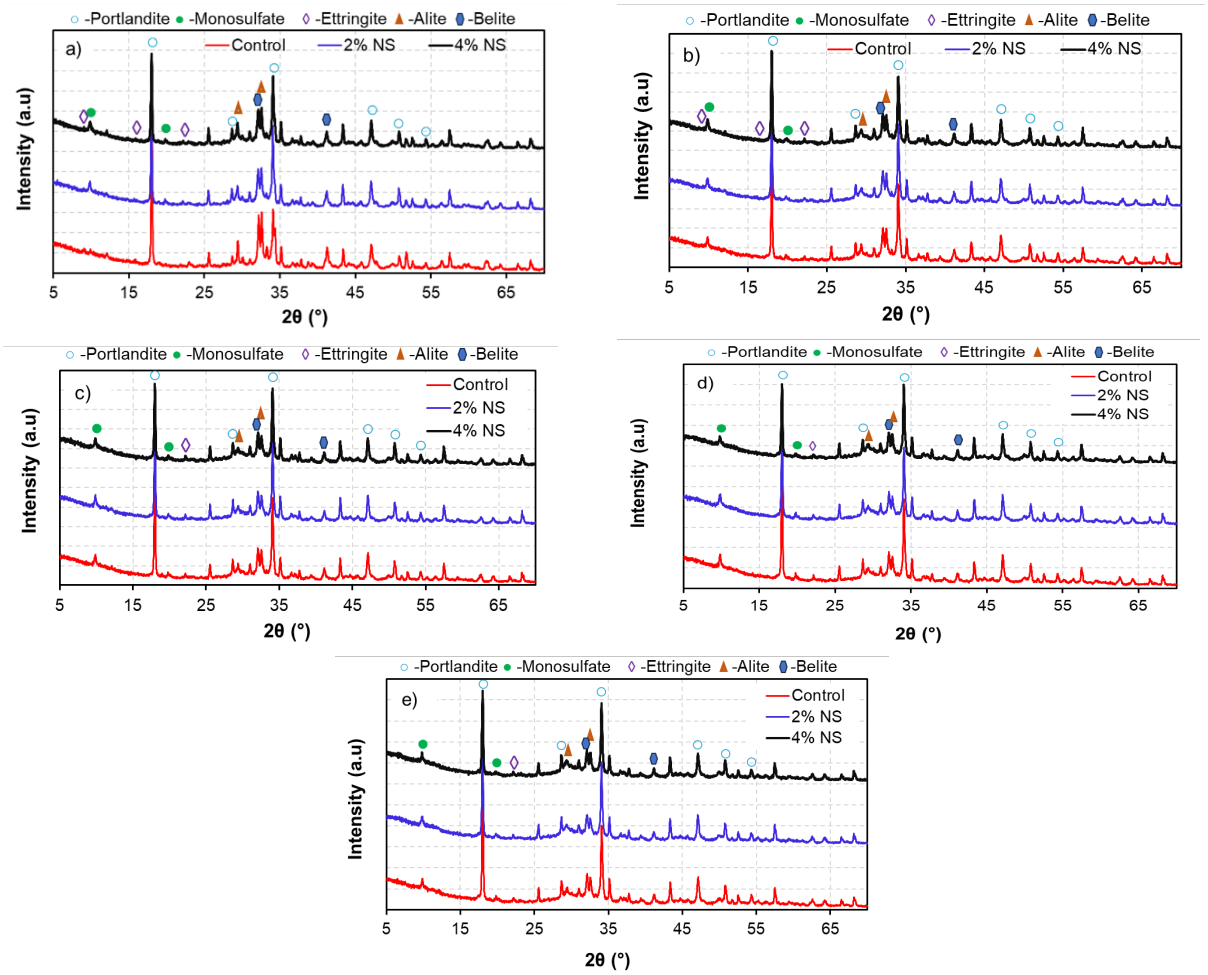

578

579 **Fig. 8.** X-ray diffraction curves of the cement pastes at (a) one, (b) three, (c) seven, (d) 28, and (e)

580 56 days.

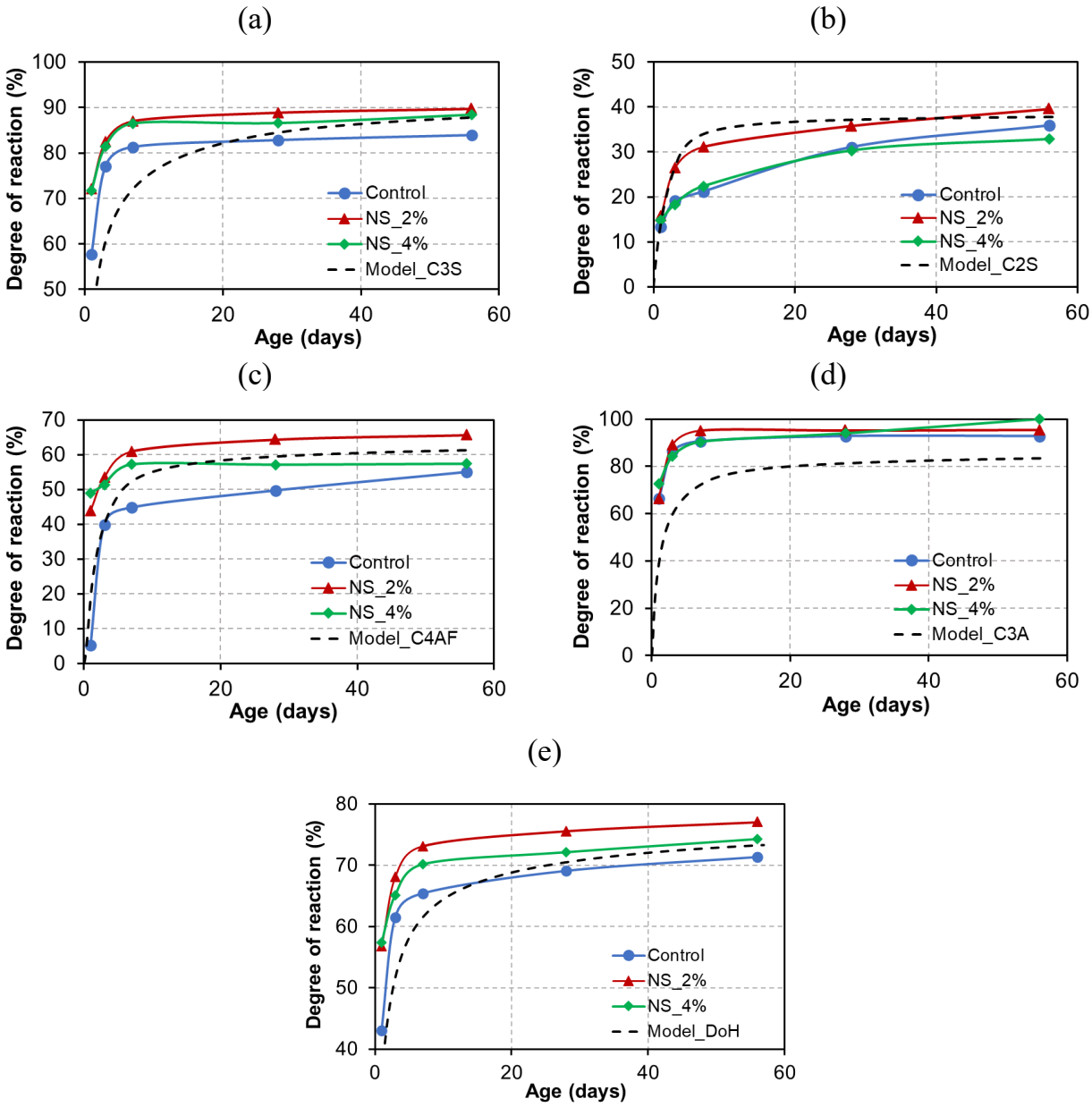

Fig. 9. Reaction degree of clinker minerals in the cement pastes: (a) C_3S, (b) C_2S, (c) C_3A, and (d) C_4AF. (e) Overall hydration degree of cement pastes.

4.2 Analysis of microstructures

SEM utilising backscattered electron (SEM-BSE) imaging was employed to analyse the cement paste with (2% by weight) and without nano-silica at aging intervals of three and seven days. This investigation aims to determine the influence of nano-silica on the microstructures of cement pastes. The SEM micrographs of the pastes are shown in **Fig. 10**. The increase in the number of nucleation sites facilitated by nano-silica substitution is prominent in the initial stages, as indicated by the

degradation of the portlandite (CH) surface in **Fig. 9**(b). Moreover, replacing nano-silica yielded a more compact microstructure within the cement paste. This microstructural change is due to the pozzolanic effect of nano-silica [86], which triggers a secondary hydration reaction.

Consequently, this secondary reaction leads to the formation of supplementary calcium silicate hydrate (C-S-H) through the consumption of portlandite (**Fig. 9**(d)). The increased density of the microstructure can also be attributed to the filling effect exhibited by nano-silica. Considering ultrafine particles, nano-silica effectively occupied the pores within the cement paste, contributing to the overall densification.

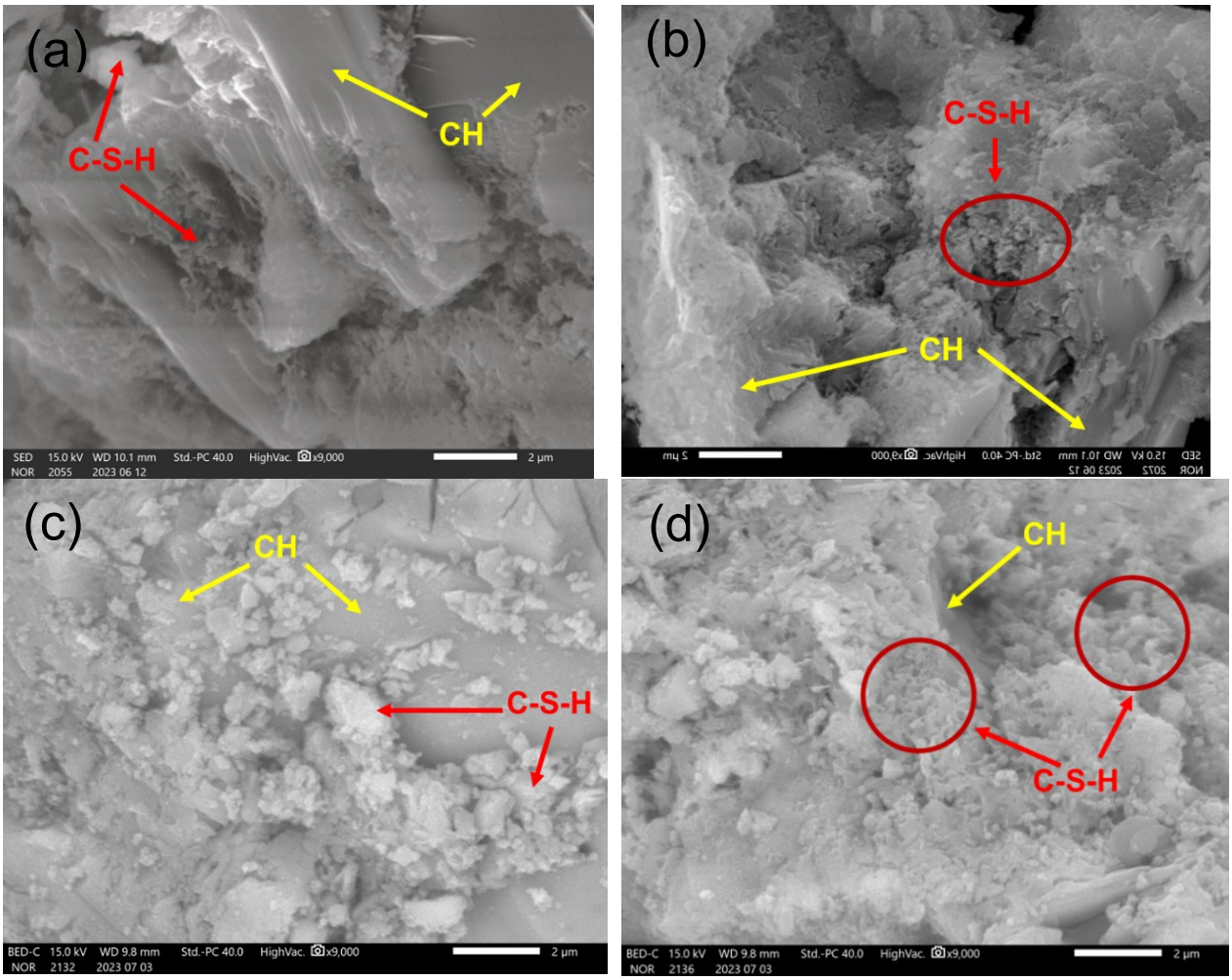

Fig. 10. SEM-BSE micrographs of (a and b) control paste, at days one and seven, respectively, and (c and d) 2% nano-silica substituted paste at days one and seven, respectively.

603 The impact of substituting nano-silica on the chemical composition of the resulting hydrates was
604 investigated using elemental composition analysis (SEM-EDS). EDS analysis points were chosen by
605 visual distinctions in the grey scale intensities within the backscattered electron (BSE) images and
606 significant elevations in the intensities of the major elements (Ca, Si, and Al) in the EDS maps.
607 Approximately 50 specific points were targeted during EDS point analysis to capture the atomic ratios
608 of Ca, Si, and Al. **Fig. 11** depicts the distribution of the Al/Ca and Si/Ca ratios within the C-S-H phase
609 of the control sample and sample with 2% nano-silica after seven days. A particular trend emerged
610 with points exhibiting an upward shift upon nano-silica substitution. This trend, resulting in an
611 increased silicon-to-calcium (Si/Ca) ratio as the Si content in the paste increased, was attributed to
612 the presence of Si, originating from nano-silica. The Al/Ca and Si/Ca ratios within the primary C-S-
613 H phase, encompassing both inner and outer regions, span broad ranges of 0.03–0.25 and 0.21–0.52,
614 respectively.
615 Furthermore, an increase in the Al/Ca ratio, which was noted within additional secondary C-S-H
616 formations, was attributed to the pozzolanic reaction of nano-silica. In this scenario, the C-S-H
617 structure absorbs Al in lieu of Si. This finding aligns with the prior literature [2,50,87], demonstrating
618 the emergence of C-S-H structures at elevated Si/Ca ratios, reminiscent of tobermorite-like structures.
619 Therefore, the Si/Ca ratios of the nano-silica substituted samples were considered to be 0.67, which
620 is slightly higher than that of the control sample (0.58). Furthermore, partially reacted nano-silica was
621 characterised by elevated Si/Ca and reduced Al/Ca ratios (**Fig. 11**) [87].
622 In contrast, fully reacted nano-silica induced the creation of an additional secondary C-S-H phase
623 through pozzolanic reactions. This variant of secondary C-S-H demonstrated a tendency to absorb or
624 incorporate a greater quantity of alkali, which was attributed to the negative surface charge of C-S-
625 H. Collectively, the results obtained through TGA, XRD, and SEM assays validate the favourable
626 influence of nano-silica substitution on the characteristics of cement paste. This advantageous impact
627 can be attributed to the synergistic effects of the nucleation and pozzolanic reactions induced by nano-
628 silica. To comprehensively capture and simulate this phenomenon and ensuring a realistic

representation of the intricate influence exerted by nano-silica, this phenomenon was carefully incorporated into the coupled hydration and thermodynamic model, as explained in Section 3.1.

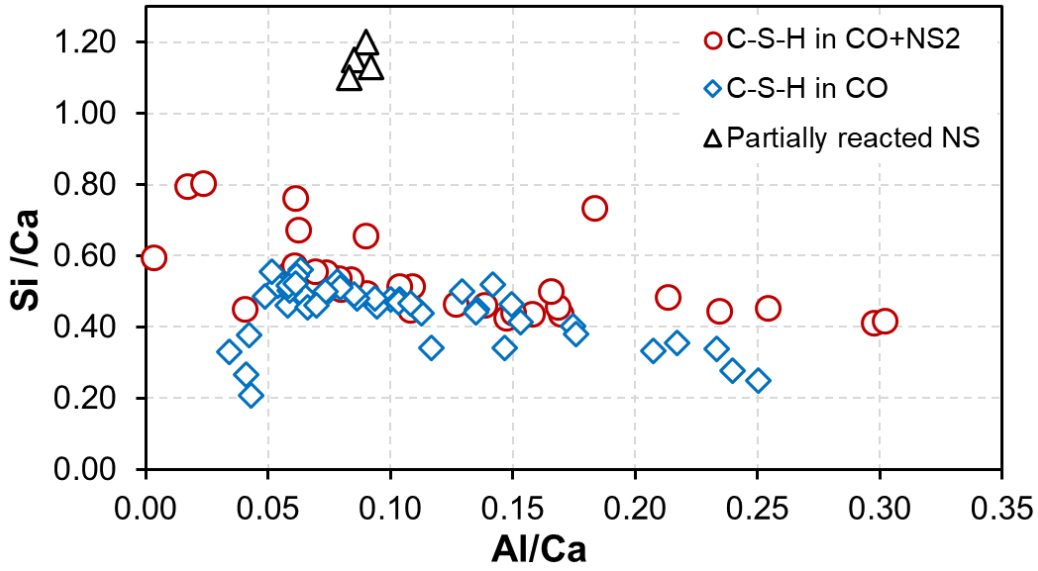

Fig. 11. Variation of Al/Ca and Si/Ca ratios of C-S-H structure found in control paste and 2% nano-silica containing paste at 7 days.

4.3 Prediction of volume fraction of hydrates with hydration time

Following the discussion in Section 3.2, the volume fractions of the phases, namely hydrated, unhydrated, unreacted nano-silica, chemical shrinkage, and capillary pores, were estimated as functions of the hydration age. The predictions are shown in **Fig. 12**. The most significant increase in the volume fractions of the hydrates, particularly C-S-H, was observed with the substitution of 2% nano-silica (**Fig. 12**(a)), regardless of the hydration age. **Fig. 12**(b) shows a gradual reduction in the unhydrated phases in all pastes (CO, CO + NS2, and CO + NS4) as hydration progressed. Notably, there is a linear relationship between the volume fractions of the unhydrated phases in the mixtures. These results clearly indicate that hydration of clinker minerals remained independent of the nano-silica reactivity; instead, it was solely governed by the initial cement content present in each specific mixture. The changes in the volume fractions of the pore phases with hydration age are illustrated in **Fig. 12**(c), as discussed in Section 3.2. The findings reveal a steady reduction in the pores within the

cement paste containing nano-silica, compared to those without nano-silica, at all stages of hydration. This phenomenon was attributed to the denser microstructure resulting from the incorporation of nano-silica.

Additionally, the ultra-fine nano-silica particles acted as a filler material, contributing to decreased porosity within the cement paste. **Fig. 12**(d) illustrates the relationship between the volume fraction of unreacted nano-silica and hydration age of the different pastes. Unreacted nano-silica increased proportional to the initial nano-silica content in the cement paste. However, within a specific cement paste, the unreacted nano-silica content diminished as hydration progressed, owing to the increasing contribution of nano-silica to the pozzolanic reactions over time. Considering the overall reactivity of nano-silica in the cement paste, the optimal replacement ratio was determined to be 2%.

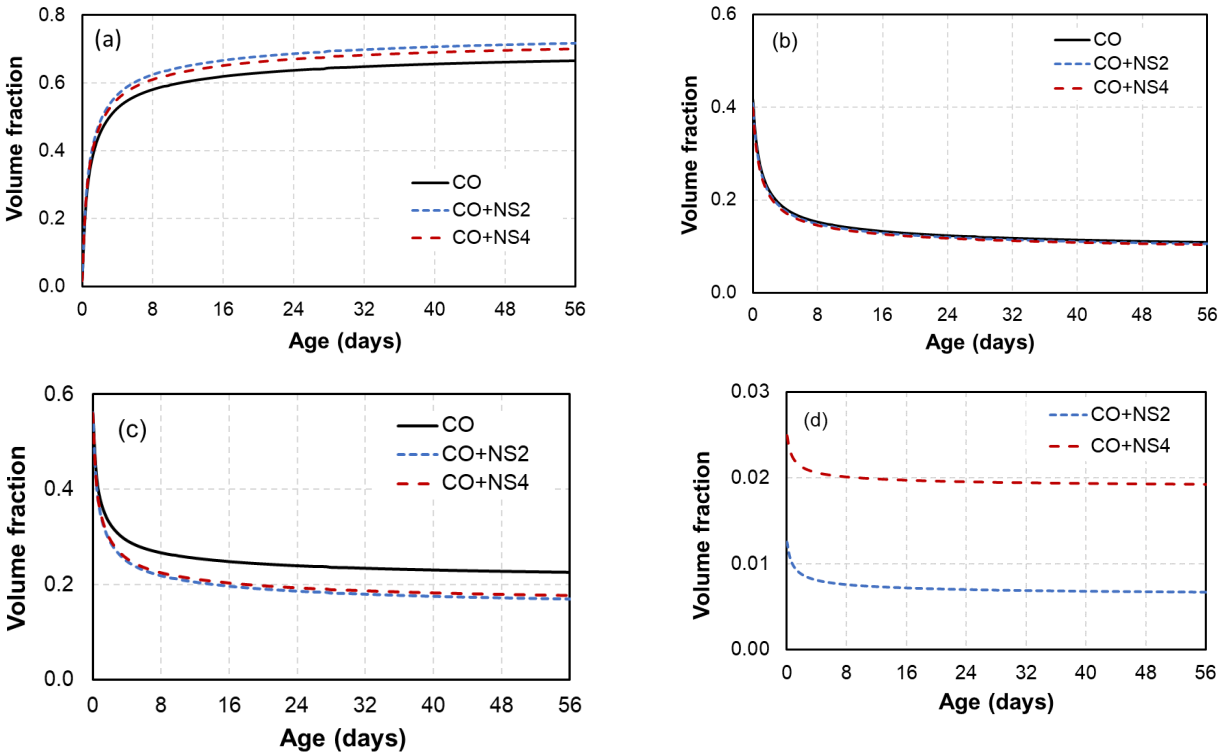

Fig. 12. Volume fraction of (a) hydrated phase, (b) unhydrated phase, (c) pore phase, and (d) unreacted nano-silica of the cement pastes.

664 **4.4 Finite element model verification**

665 As outlined in Section 3.4, the numerical microstructure (RVE) generated for the seven-day aged
666 cement paste without nano-silica incorporation was examined using various mesh sizes. The predicted
667 compressive strengths are shown in **Fig. 13**. The simulations revealed that the compressive strength
668 of the cement paste exhibited limited sensitivity to changes in the mesh size (**Fig. 13**). Nevertheless,
669 reducing the mesh size led to decreased variability in the predicted compressive strengths, consistent
670 with theoretical expectations [88]. Therefore, for the sake of result consistency, unless otherwise
671 stated, a fine mesh was selected for all the analyses in this study.

672

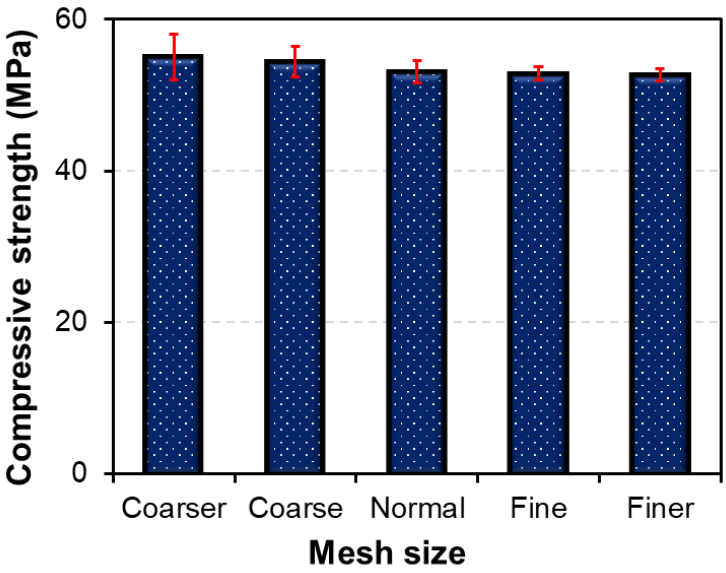

673

674 **Fig. 13.** Results of the mesh convergency study of the control paste at day seven.

675

676 Because the homogenisation of materials with randomly distributed inclusions affects localised
677 deformation and leads to inaccurate computation of mechanical properties, stress-strain responses
678 were simulated for five distinct configurations of unhydrated particles and pores within the hydrated
679 paste. **Fig. 14** depicts the stress-strain responses of these random configurations with the mean stress-
680 strain response, revealing standard deviations of 1.6 MPa and 0.4 Gpa for homogenised compressive
681 strength and Young's modulus, respectively. These values align with those in the existing literature

682 [89] and suggest that approximately five random samples are generally sufficient to determine the
683 mean mechanical properties.

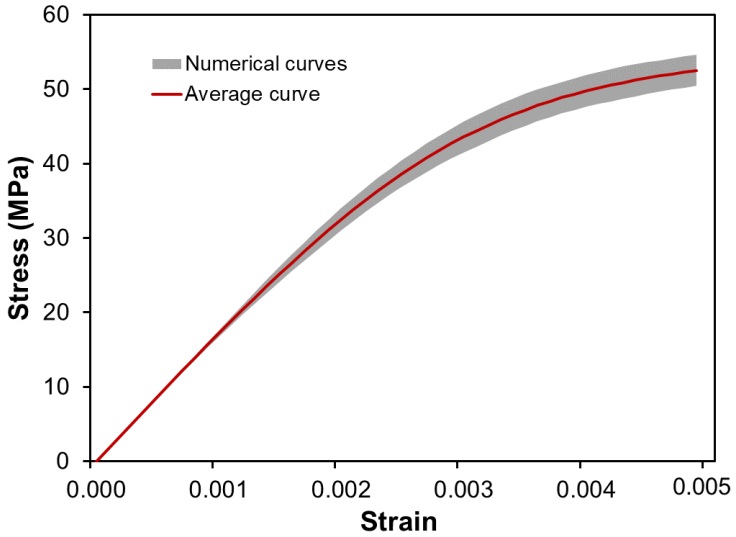

684

685 **Fig. 14.** Stress-strain behaviour of a random RVE, corresponding to the control paste at day seven.

686

687 **Fig. 15** illustrates the computed stress-strain curves for the cement paste with (2 and 4%) and without
688 nano-silica after seven days of aging. Furthermore, the stress distributions depicting the plastic
689 potential at the strain values of 0.002 and 0.004 for each RVE are shown in **Fig. 16**. A comparison of
690 the microstructures with and without nano-silica at 0.002 strain (**Fig. 16**(a–c)) reveals that the cement
691 paste without nano-silica exhibits higher plastic potential values across the microstructure, indicative
692 of ductile behaviour [90]. Conversely, the incorporation of nano-silica reinforced the microstructure
693 and reduced the plastic potential. As a result, nano-silica-reinforced cement pastes demonstrated a
694 higher Young's modulus and strength (**Fig. 15**) than the control cement paste, which was more prone
695 to deformation under stress.
696 Similarly, when examining the microstructure of the pastes at a strain of 0.004, the cement paste with
697 nano-silica exhibited increased pore closure (depicted by a larger red area) compared to the control
698 paste, due to compressive stress. This enhanced pore closure increases the effective load transfer area
699 between the microstructural elements, thereby reducing the stress concentration areas and enhancing
700 the strength of the material (**Fig. 15**) [91]. Additionally, the increased strength was accompanied by

a more significant ultimate deformation (**Fig. 16**(e–f)); nano-silica further influenced the nonlinear behaviour by augmenting the nonlinear deformation capacity of the material. Thus, it can be concluded that the developed RVE and microscale finite element analysis can realistically predict the influence of nano-silica in cement pastes, elucidating its role in enhancing both mechanical strength and nonlinear behaviour.

As the experimental compression tests in this study focused solely on capturing the ultimate compressive strength, the entire stress-strain response was comprehensively compared with those in other studies [92,93] that reported similar compressive behaviours.

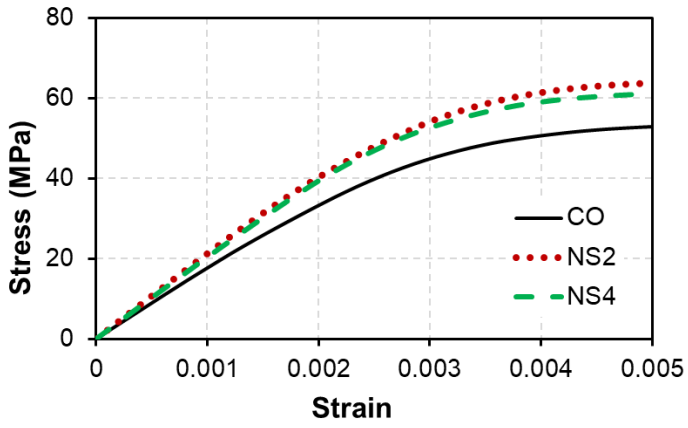

Fig. 15. Stress-strain response of the control paste (CO) aged for seven days and pastes containing nano-silica (NS2 and NS4)

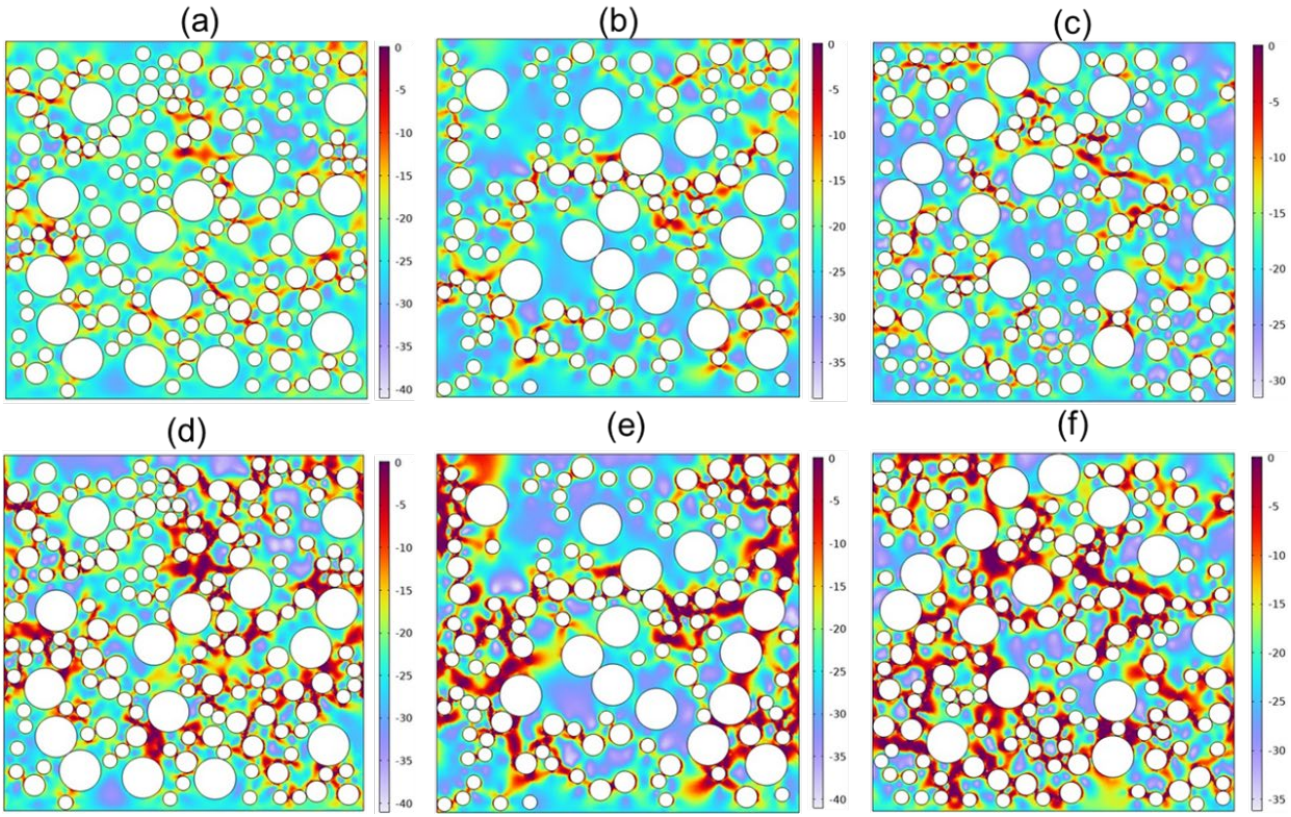

Fig. 16. Stress distribution (plastic potential) of seven-day aged pastes: (a) control, (b) 2% nano-silica containing, and (c) 4% nano-silica containing pastes at strain values of 0.002 and (d) control, (e) 2% nano-silica containing, and (f) 4% nano-silica containing pastes at strain values of 0.004.

The compressive strengths of all cement pastes across different ages are shown in **Fig. 17**. Notably, a significant improvement in strength compared to the control paste was observed with increasing concentrations of nano-silica substitution. This effect, which was particularly prominent during the early stages of hydration, was attributed to nucleation and pozzolanic influences. This effect resulted in the significant presence of hydrated phases (C-S-H), which are the primary contributors to strength development in cement pastes [6]. However, when substituted with 4% nano-silica, the compressive strength decreased compared to that achieved with 2% substitution. This outcome can be attributed to the agglomeration of nano-silica particles (Section 4.2), which impedes the hydration process and results in the formation of hydration products such as C-S-H. Furthermore, the model slightly underestimated the compressive strength for all samples at an age of one day (**Fig. 17)**. This can be

attributed to the inferior mechanical properties of the cement matrix due to incomplete hydration and higher volume fraction of the pore phase, which collectively lead to a weaker matrix that is less capable of withstanding higher loads.

Nonetheless, the experimental findings indicate that substituting 2% nano-silica increases the compressive strength by 35.2, 21.2, and 17.2% at days one, three, and seven, respectively. In contrast, 4% nano-silica substitution resulted in compressive strength increase of 17.8, 7.6, and 15.9%, at days one, three, and seven, respectively. This trend aligns closely with the predictions of the proposed numerical model.

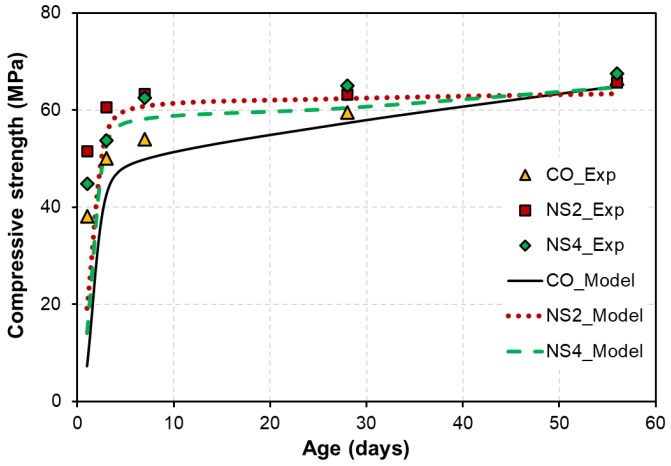

Fig. 17. Comparison of compressive strength values from experimental and numerical models.

The variation in the Young's modulus with hydration age is depicted in **Fig. 18**. The predicted values have not been compared with experimental results since only the ultimate compressive strength was captured during the experimental tests. Nevertheless, **Fig. 18** illustrates that substituting nano-silica into cement paste increases the Young's modulus, indicating improved stiffness and resistance to deformation. This enhancement is attributed to the stronger interparticle bonding and cohesion facilitated by nano-silica [5,16], which bridges the gaps between the cement particles. Furthermore, the filling of nanoscale voids and porosity reduction contributed to a denser microstructure [18], ultimately enhancing the rigidity of the material.

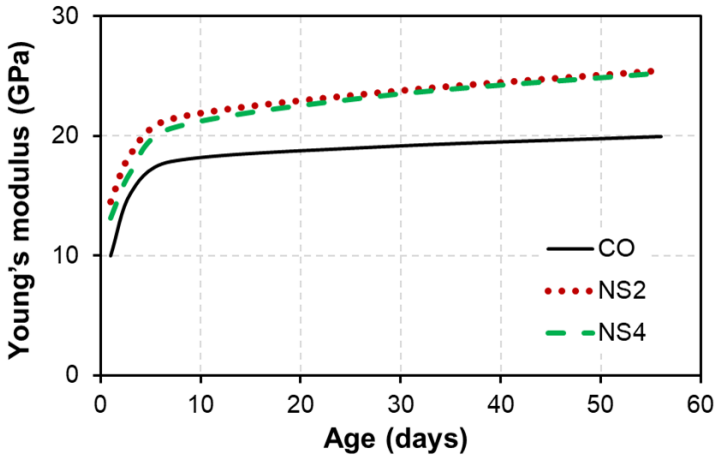

748

749 **Fig. 18**. Predicted Young's modulus of the cement pastes with respect to hydration age.

750

751 **5. Conclusions**

752 This study introduced a coupled hydration and thermodynamic model to optimise nano-silica
753 replacement in nano-silica reinforced cement paste and proposed a numerical approach to predict its
754 nonlinear behaviour. Furthermore, the predicted results were verified using experimental results. The
755 following conclusions were drawn based on both numerical and experimental results.

756

757 1. A coupled hydration and thermodynamic model was proposed to predict the volume fractions
758 of the phases, such as hydrates, unhydrated clinker, pores, and unreacted nano-silica, in cement pastes
759 with and without including nano-silica over varying hydration times. This model was implemented
760 using the PHREEQC-MATLAB interface. Subsequently, the predicted results were validated against
761 the experimental data.

762 2. Replacing cement with nano-silica in cement pastes significantly enhanced the mechanical
763 properties of the nano-silica-reinforced cement pastes. This improvement stems from the synergistic
764 effects of nucleation and pozzolanic reactions. Through numerical simulations and experimental
765 observations, the optimal replacement level was determined to be 2% by the weight of the cement
766 content.

3. A cement paste RVE was developed in MATLAB based on the predicted phase volume fraction, while accounting for the hydration of clinker particles and agglomeration of nano-silica particles.

4. Finite element analysis was conducted on the developed RVE using COMSOL Multiphysics software by incorporating suitable boundary conditions. This analysis predicted the nonlinear behaviour of pastes with and without nano-silica. The introduction of nano-silica significantly improved the strength and deformation capacity of the paste under compression.

5. The mechanical properties, such as the compressive strength and Young's modulus, of the pastes with and without nano-silica were predicted, and the values were consistent with the experimental values.

6. Refining the proposed models to accurately depict the dispersion and agglomeration of nano-silica in numerical simulations offered a more intricate and comprehensive understanding of the material behaviour. This enhancement enabled a more precise assessment of the impact of nano-silica on the mechanical properties of cement paste, leading to further insights and advancements in material science.

Declaration of Competing Interest

The authors declare that they have no known competing financial interests or personal relationships that could have appeared to influence the work reported in this paper.

Acknowledgement

This study was supported by JST SPRING under Grant Number JPMJSP2119.

References

[1] Makul N. Modern sustainable cement and concrete composites: Review of current status, challenges and guidelines. Sustainable Materials and Technologies 2020;25. https://doi.org/10.1016/j.susmat.2020.e00155.

[2] Lothenbach B, Scrivener K, Hooton RD. Supplementary cementitious materials. Cem Concr Res 2011;41:1244–56. https://doi.org/10.1016/j.cemconres.2010.12.001.

[3] Akhnoukh AK, Elia H. Developing high performance concrete for precast/prestressed concrete industry. Case Studies in Construction Materials 2019;11. https://doi.org/10.1016/j.cscm.2019.e00290.

[4] Khan K, Ahmad W, Amin MN, Nazar S. Nano-Silica-Modified Concrete: A Bibliographic Analysis and Comprehensive Review of Material Properties. Nanomaterials 2022;12. https://doi.org/10.3390/nano12121989.

[5] Snehal K, Das BB, Akanksha M. Early age, hydration, mechanical and microstructure properties of nano-silica blended cementitious composites. Constr Build Mater 2020;233:117212. https://doi.org/10.1016/j.conbuildmat.2019.117212.

[6] Praveen Kumar VV, Dey S. Study on strength and durability characteristics of nano-silica based blended concrete. Hybrid Advances 2023;2:100011. https://doi.org/10.1016/j.hybadv.2022.100011.

[7] Singh LP, Ali D, Tyagi I, Sharma U, Singh R, Hou P. Durability studies of nano-engineered fly ash concrete. Constr Build Mater 2019;194:205–15. https://doi.org/10.1016/j.conbuildmat.2018.11.022.

[8] Liu X, Hou P, Chen H. Effects of nanosilica on the hydration and hardening properties of slag cement. Constr Build Mater 2021;282. https://doi.org/10.1016/j.conbuildmat.2021.122705.

[9] Chithra S, Senthil Kumar SRR, Chinnaraju K. The effect of Colloidal Nano-silica on workability, mechanical and durability properties of High Performance Concrete with Copper slag as partial fine aggregate. Constr Build Mater 2016;113:794–804. https://doi.org/10.1016/j.conbuildmat.2016.03.119.

[10] Cai Y, Xuan D, Poon CS. Effects of nano-SiO2 and glass powder on mitigating alkali-silica reaction of cement glass mortars. Constr Build Mater 2019;201:295–302. https://doi.org/10.1016/j.conbuildmat.2018.12.186.

[11] Raheem AA, Abdulwahab R, Kareem MA. Incorporation of metakaolin and nanosilica in blended cement mortar and concrete- A review. J Clean Prod 2021;290. https://doi.org/10.1016/j.jclepro.2021.125852.

[12] Lin RS, Oh S, Du W, Wang XY. Strengthening the performance of limestone-calcined clay cement (LC3) using nano silica. Constr Build Mater 2022;340. https://doi.org/10.1016/j.conbuildmat.2022.127723.

[13] Hou P, Kawashima S, Kong D, Corr DJ, Qian J, Shah SP. Modification effects of colloidal nanoSiO2 on cement hydration and its gel property. Compos B Eng 2013;45:440–8. https://doi.org/10.1016/j.compositesb.2012.05.056.

[14] Meng T, Ying K, Hong Y, Xu Q. E ff ect of di ff erent particle sizes of nano - SiO 2 on the properties and microstructure of cement paste 2020:833–42.

[15] Kooshafar M, Madani H. An investigation on the influence of nano silica morphology on the characteristics of cement composites. Journal of Building Engineering 2020;30:101293. https://doi.org/10.1016/j.jobe.2020.101293.

[16] Senff L, Labrincha JA, Ferreira VM, Hotza D, Repette WL. Effect of nano-silica on rheology and fresh properties of cement pastes and mortars. Constr Build Mater 2009;23:2487–91. https://doi.org/10.1016/j.conbuildmat.2009.02.005.

840 [17] Qing Y, Zenan Z, Deyu K, Rongshen C. Influence of nano-SiO2 addition on properties of
841 hardened cement paste as compared with silica fume. Constr Build Mater 2007;21:539–45.
842 https://doi.org/10.1016/j.conbuildmat.2005.09.001.

843 [18] Stefanidou M, Papayianni I. Influence of nano-SiO 2 on the Portland cement pastes. Compos
844 B Eng 2012;43:2706–10. https://doi.org/10.1016/j.compositesb.2011.12.015.

845 [19] Haruehansapong S, Pulngern T, Chucheepsakul S. Effect of the particle size of nanosilica on
846 the compressive strength and the optimum replacement content of cement mortar containing
847 nano-SiO2. Constr Build Mater 2014;50:471–7.
848 https://doi.org/10.1016/j.conbuildmat.2013.10.002.

849 [20] Abhilash PP, Nayak DK, Sangoju B, Kumar R, Kumar V. Effect of nano-silica in concrete; a
850 review. Constr Build Mater 2021;278:122347.
851 https://doi.org/10.1016/j.conbuildmat.2021.122347.

852 [21] Ali R, Muayad M, Mohammed AS, Asteris PG. Analysis and prediction of the effect of
853 Nanosilica on the compressive strength of concrete with different mix proportions and
854 specimen sizes using various numerical approaches. Structural Concrete 2022.
855 https://doi.org/10.1002/suco.202200718.

856 [22] Sun J, Ma Y, Li J, Zhang J, Ren Z, Wang X. Machine learning-aided design and prediction of
857 cementitious composites containing graphite and slag powder. Journal of Building Engineering
858 2021;43:102544. https://doi.org/10.1016/J.JOBE.2021.102544.

859 [23] Bishnoi S, Scrivener KL. μic: A new platform for modelling the hydration of cements. Cem
860 Concr Res 2009;39:266–74. https://doi.org/10.1016/J.CEMCONRES.2008.12.002.

861 [24] Tolman FP. CEMHYD3D: A Three-Dimensional Cement Hydration and Microstructure
862 Development Modeling Package. Autom Constr 1999;8:227–235.

[25] Nithurshan M, Elakneswaran Y. A Systematic Review and Assessment of Concrete Strength Prediction Models. Case Studies in Construction Materials 2023;18:e01830. https://doi.org/10.1016/j.cscm.2023.e01830.

[26] Jennings HM, Johnson SK. Simulation of Microstructure Development During the Hydration of a Cement Compound. Journal of the American Ceramic Society 1986;69:790–5. https://doi.org/10.1111/J.1151-2916.1986.TB07361.X.

[27] Maekawa K, Ishida T, Kishi T. Multi-Scale Modeling of Structural Concrete. Multi-Scale Modeling of Structural Concrete 2008:1–655. https://doi.org/9781482288599.

[28] Kavvadias IE, Tsongas K, Bantilas KE, Falara MG, Thomoglou AK, Gkountakou FI, et al. Mechanical Characterization of MWCNT-Reinforced Cement Paste: Experimental and Multiscale Computational Investigation. Materials 2023;16:5379. https://doi.org/10.3390/ma16155379.

[29] Quercia G, Hüsken G, Brouwers HJH. Water demand of amorphous nano silica and its impact on the workability of cement paste. Cem Concr Res 2012;42:344–57. https://doi.org/10.1016/j.cemconres.2011.10.008.

[30] Elkady H, Serag M, Elfeky M. Effect of Nano Silica De-agglomeration, and Methods of Adding Super-plasticizer on the Compressive Strength, and Workability of Nano Silica Concrete. Civil & Environmental … 2013;3:21–35.

[31] Wang L, Zheng D, Zhang S, Cui H, Li D. Effect of nano-SiO2 on the hydration and microstructure of Portland cement. Nanomaterials 2016;6. https://doi.org/10.3390/nano6120241.

[32] Xu Y, Liu M, Li P, Zhu L, Xia X, Zhang C, et al. Effect of dispersant types on the rheological and mechanical properties of oil well cement paste with nanosilica. Constr Build Mater 2021;271. https://doi.org/10.1016/j.conbuildmat.2020.121576.

[33] Maruyama I, Igarashi G. Cement reaction and resultant physical properties of cement paste. Journal of Advanced Concrete Technology 2014;12:200–13. https://doi.org/10.3151/jact.12.200.

[34] Lothenbach B, Zajac M. Application of thermodynamic modelling to hydrated cements. Cem Concr Res 2019;123. https://doi.org/10.1016/j.cemconres.2019.105779.

[35] Elakneswaran Y, Owaki E, Miyahara S, Ogino M, Maruya T, Nawa T. Hydration study of slag-blended cement based on thermodynamic considerations. Constr Build Mater 2016;124:615–25. https://doi.org/10.1016/j.conbuildmat.2016.07.138.

[36] Elakneswaran Y, Owaki E, Miyahara S, Ogino M, Maruya T, Nawa T. Hydration study of slag-blended cement based on thermodynamic considerations. Constr Build Mater 2016;124:615–25. https://doi.org/10.1016/j.conbuildmat.2016.07.138.

[37] Parkhurst DL, Appelo CAJ. USER'S GUIDE TO PHREEQC (VERSION 2)-A COMPUTER PROGRAM FOR SPECIATION, BATCH-REACTION, ONE-DIMENSIONAL TRANSPORT, AND INVERSE GEOCHEMICAL CALCULATIONS. n.d.

[38] Lothenbach B, Kulik DA, Matschei T, Balonis M, Baquerizo L, Dilnesa B, et al. Cemdata18: A chemical thermodynamic database for hydrated Portland cements and alkali-activated materials. Cem Concr Res 2019;115:472–506. https://doi.org/10.1016/j.cemconres.2018.04.018.

[39] Singh LP, Bhattacharyya SK, Shah SP, Mishra G, Sharma U. Studies on early stage hydration of tricalcium silicate incorporating silica nanoparticles: Part II. Constr Build Mater 2016;102:943–9. https://doi.org/10.1016/j.conbuildmat.2015.05.084.

[40] Scrivener K, Ouzia A, Juilland P, Kunhi Mohamed A. Advances in understanding cement hydration mechanisms. Cem Concr Res 2019;124. https://doi.org/10.1016/j.cemconres.2019.105823.

[41] Singh LP, Zhu W, Howind T, Sharma U. Quantification and characterization of C-S-H in silica nanoparticles incorporated cementitious system. Cem Concr Compos 2017;79:106–16. https://doi.org/10.1016/j.cemconcomp.2017.02.004.

[42] Parrot LJ, Killoh DC. Prediction of cement hydration. Proceedings of the British Ceramic Society, 1984, p. 41–53.

[43] Krishnya S, Yoda Y, Elakneswaran Y. A two-stage model for the prediction of mechanical properties of cement paste. Cem Concr Compos 2021;115:103853. https://doi.org/10.1016/J.CEMCONCOMP.2020.103853.

[44] Lothenbach B, Matschei T, Möschner G, Glasser FP. Thermodynamic modelling of the effect of temperature on the hydration and porosity of Portland cement. Cem Concr Res 2008;38:1–18. https://doi.org/10.1016/j.cemconres.2007.08.017.

[45] Lothenbach B, Winnefeld F. Thermodynamic modelling of the hydration of Portland cement. Cem Concr Res 2006;36:209–26. https://doi.org/10.1016/j.cemconres.2005.03.001.

[46] Bentz DP, Waller V, De Larrard F. PREDICTION OF ADIABATIC TEMPERATURE RISE IN CONVENTIONAL AND HIGH-PERFORMANCE CONCRETES USING A 3-D MICROSTRUCTURAL MODEL. 1998.

[47] Waller V. Doctorat de l'École Nationale des Ponts et Chaussées Spécialité Structures et Matériaux Thèse présentée par. n.d.

[48] Tennis PD, Jennings HM. A model for two types of calcium silicate hydrate in the microstructure of Portland cement pastes. n.d.

[49] Constantinides G, Ulm FJ. The effect of two types of C-S-H on the elasticity of cement-based materials: Results from nanoindentation and micromechanical modeling. Cem Concr Res 2004;34:67–80. https://doi.org/10.1016/S0008-8846(03)00230-8.

[50] Richardson IG. Tobermorite/jennite- and tobermorite/calcium hydroxide-based models for the structure of C-S-H: Applicability to hardened pastes of tricalcium silicate, β-dicalcium silicate, Portland cement, and blends of Portland cement with blast-furnace slag, metakaolin, or silica fume. Cem Concr Res 2004;34:1733–77. https://doi.org/10.1016/j.cemconres.2004.05.034.

[51] Idiart A, Bisschop J, Caballero A, Lura P. A numerical and experimental study of aggregate-induced shrinkage cracking in cementitious composites. Cem Concr Res 2012;42:272–81. https://doi.org/10.1016/j.cemconres.2011.09.013.

[52] Ishida T, Maekawa K. Simulation of Early-Age Cracking due to Drying Shrinkage Based on a Multi-Scale Constitutive Model Biaxial shear View project Technical developoment of UHPFRC bridge in Japan View project Tetsuya Mishima Maeda Corporation 2013. https://doi.org/10.1061/9780784412992.069.

[53] Dale P. Bentz, Pietro Lura, John W. Roberts. Mixture Proportioning for Internal Curing. Concrete International 2005;35:35–40.

[54] B.Y.D.P. Bentz PLJWR. Mixture proportioning for internal curing. Concrete International 2005:35–40.

[55] Powers TC, Brownyard TL. Studies of the Physical Properties of Hardened Portland Cement Paste. Journal Proceedings 1946;43:101–32. https://doi.org/10.14359/8745.

[56] Zhang M, Jivkov AP. Microstructure-informed modelling of damage evolution in cement paste. Constr Build Mater 2014;66:731–42. https://doi.org/10.1016/j.conbuildmat.2014.06.017.

[57] Wu Z, Zhang J, Fang Q, Yu H, Haiyan M. Mesoscopic modelling of concrete material under static and dynamic loadings: A review. Constr Build Mater 2021;278:122419. https://doi.org/10.1016/j.conbuildmat.2021.122419.

956 [58] Chen H, Xu B, Mo YL, Zhou T. Behavior of meso-scale heterogeneous concrete under uniaxial
957 tensile and compressive loadings. Constr Build Mater 2018;178:418–31.
958 https://doi.org/10.1016/j.conbuildmat.2018.05.052.

959 [59] Wriggers P, Moftah SO. Mesoscale models for concrete: Homogenisation and damage
960 behaviour. Finite Elements in Analysis and Design 2006;42:623–36.
961 https://doi.org/10.1016/j.finel.2005.11.008.

962 [60] Rupasinghe M. An investigation of strength and hydration characteristics of nano-silica
963 incorporated concrete. The University of Melbourne, 2015.

964 [61] Pal B, Ramaswamy A. Mechanics of Materials A multi-physics-based approach to predict
965 mechanical behavior of concrete element in a multi-scale framework. Mechanics of Materials
966 2023;176:104509. https://doi.org/10.1016/j.mechmat.2022.104509.

967 [62] Wang X, Yang Z, Jivkov AP. Monte Carlo simulations of mesoscale fracture of concrete with
968 random aggregates and pores: A size effect study. Constr Build Mater 2015;80:262–72.
969 https://doi.org/10.1016/j.conbuildmat.2015.02.002.

970 [63] Rupasinghe M, San Nicolas R, Mendis P, Sofi M, Ngo T. Investigation of strength and
971 hydration characteristics in nano-silica incorporated cement paste. Cem Concr Compos
972 2017;80:17–30. https://doi.org/10.1016/J.CEMCONCOMP.2017.02.011.

973 [64] Skaryński L, Tejchman J. Calculations of fracture process zones on meso-scale in notched
974 concrete beams subjected to three-point bending. European Journal of Mechanics, A/Solids
975 2010;29:746–60. https://doi.org/10.1016/j.euromechsol.2010.02.008.

976 [65] Kim SM, Abu Al-Rub RK. Meso-scale computational modeling of the plastic-damage response
977 of cementitious composites. Cem Concr Res 2011;41:339–58.
978 https://doi.org/10.1016/j.cemconres.2010.12.002.

979 [66] Zhang H. Building materials in civil engineering. Elsevier Ltd; 2011.

[67] Haecker CJ, Garboczi EJ, Bullard JW, Bohn RB, Sun Z, Shah SP, et al. Modeling the linear elastic properties of Portland cement paste. Cem Concr Res 2005;35:1948–60. https://doi.org/10.1016/J.CEMCONRES.2005.05.001.

[68] Wang XF, Yang ZJ, Yates JR, Jivkov AP, Zhang C. Monte Carlo simulations of mesoscale fracture modelling of concrete with random aggregates and pores. Constr Build Mater 2015;75:35–45. https://doi.org/10.1016/j.conbuildmat.2014.09.069.

[69] Bentz DP. Modelling cement microstructure: Pixels, particles, and property prediction. Materials and Structures/Materiaux et Constructions 1999;32:187–95. https://doi.org/10.1007/BF02481514.

[70] Cappelli L, Montemurro M, Dau F, Guillaumat L. Multi-scale identification of the viscoelastic behaviour of composite materials through a non-destructive test. Mechanics of Materials 2019;137:103137. https://doi.org/10.1016/j.mechmat.2019.103137.

[71] COMSOL Multiphysics. COMSOL Multiphysics Reference Manual n.d. https://doc.comsol.com/5.5/doc/com.comsol.help.comsol/COMSOL_ReferenceManual.pdf (accessed June 27, 2023).

[72] COMSOL Multiphysics. LiveLink™ for MATLAB® User's Guide n.d. https://doc.comsol.com/5.4/doc/com.comsol.help.llmatlab/LiveLinkForMATLABUsersGuide.pdf (accessed June 27, 2023).

[73] B. Bresler, K.S. Pister. Strength of concrete under combined stress. ACI Journal 1958;551:321–45. https://doi.org/10.1016/0008-8846(71)90082-2.

[74] Hlobil M, Šmilauer V, Chanvillard G. Micromechanical multiscale fracture model for compressive strength of blended cement pastes. Cem Concr Res 2016;83:188–202. https://doi.org/10.1016/J.CEMCONRES.2015.12.003.

1003 [75] Nemecek J. Nanoindentation assisted characterization of heterogeneous structural materials.
1004 2018.

1005 [76] Nguyen VP, Stroeven M, Sluys LJ. Multiscale failure modeling of concrete: Micromechanical
1006 modeling, discontinuous homogenization and parallel computations. Comput Methods Appl
1007 Mech Eng 2012;201–204:139–56. https://doi.org/10.1016/j.cma.2011.09.014.

1008 [77] Velez K, Maximilien S, Damidot D, Fantozzi G, Sorrentino F. Determination by
1009 nanoindentation of elastic modulus and hardness of pure constituents of Portland cement
1010 clinker. Cem Concr Res 2001;31:555–61. https://doi.org/10.1016/S0008-8846(00)00505-6.

1011 [78] Kim JJ, Fan T, Taha MR. Homogenization Model Examining the Effect of Nanosilica on
1012 Concrete Strength and Stiffness: Https://DoiOrg/103141/2141-06 2010:28–35.
1013 https://doi.org/10.3141/2141-06.

1014 [79] Rupasinghe M, Mendis P, Ngo T, Nguyen TN, Sofi M. Compressive strength prediction of
1015 nano-silica incorporated cement systems based on a multiscale approach. Mater Des
1016 2017;115:379–92. https://doi.org/10.1016/j.matdes.2016.11.058.

1017 [80] Taylor HFW. Cement chemistry 2nd edition. 1997. https://doi.org/978-0-7277-4179-0.

1018 [81] Griffith A. The theory of rupture. First Int. Cong. Appl. Mech, 1924, p. 55–63.

1019 [82] Li H, Xiao HG, Yuan J, Ou J. Microstructure of cement mortar with nano-particles. Compos B
1020 Eng 2004;35:185–9. https://doi.org/10.1016/S1359-8368(03)00052-0.

1021 [83] Kim JJ, Fan T, Taha MR. Homogenization model examining the effect of nanosilica on
1022 concrete strength and stiffness. Transp Res Rec 2010:28–35. https://doi.org/10.3141/2141-06.

1023 [84] Singh LP, Ali D, Sharma U. Studies on optimization of silica nanoparticles dosage in
1024 cementitious system. Cem Concr Compos 2016;70:60–8.
1025 https://doi.org/10.1016/j.cemconcomp.2016.03.006.

[85] Flores YC, Cordeiro GC, Toledo Filho RD, Tavares LM. Performance of Portland cement pastes containing nano-silica and different types of silica. Constr Build Mater 2017;146:524–30. https://doi.org/10.1016/j.conbuildmat.2017.04.069.

[86] Sargam Y, Wang K. Influence of dispersants and dispersion on properties of nanosilica modified cement-based materials. Cem Concr Compos 2021;118. https://doi.org/10.1016/j.cemconcomp.2021.103969.

[87] Sargam Y, Wang K. Quantifying dispersion of nanosilica in hardened cement matrix using a novel SEM-EDS and image analysis-based methodology. Cem Concr Res 2021;147:106524. https://doi.org/10.1016/j.cemconres.2021.106524.

[88] Kanit T, Forest S, Galliet I, Mounoury V, Jeulin D. Determination of the size of the representative volume element for random composites: Statistical and numerical approach. Int J Solids Struct 2003;40:3647–79. https://doi.org/10.1016/S0020-7683(03)00143-4.

[89] Pelissou C, Baccou J, Monerie Y, Perales F. Determination of the size of the representative volume element for random quasi-brittle composites. Int J Solids Struct 2009;46:2842–55. https://doi.org/10.1016/j.ijsolstr.2009.03.015.

[90] Han DJ, Chen WF. A nonuniform hardening plasticity model for concrete materials. vol. 4. 1985.

[91] Higaeg M, Balać I, Grbović A, Milovančević M, Jelic M. Numerical modeling of the porosity influence on strength of structural materials. Science of Sintering 2019;51:459–67. https://doi.org/10.2298/SOS1904459H.

[92] Dede T, Ayvaz Y. Plasticity models for concrete material based on different criteria including Bresler-Pister. Mater Des 2010;31:278–86. https://doi.org/10.1016/j.matdes.2009.06.018.

[93] Nithurshan M, Elakneswaran Y, Yoda Y, Kitagaki R. A Hierarchical Approach to Evaluate The Mechanical Behaviour of Cement Paste Under Compressive Loading. Kyushu, Japan: 2023.

1050